

A granular-physics-based view of fault friction experiments

Behrooz Ferdowsi¹, Allan M. Rubin¹

¹Department of Geosciences, Princeton University, Princeton, NJ 08544, USA

Key Points:

- We examined the behavior of a sheared granular layer with time-independent contact-scale properties at and away from steady state.
- Like gouge samples in the lab, the layer mimics the rate-state friction Slip law in velocity-step and slide-hold (but not reslide) tests.
- A normalized granular temperature can be used to estimate the amplitude of the direct velocity-dependence of friction in the gouge layer.

Accepted for publication in *Journal of Geophysical Research: Solid Earth*.

Copyright 2020 American Geophysical Union.

Further reproduction or electronic distribution is not permitted.

The published version of the paper is available at <https://doi.org/10.1029/2019JB019016>

Corresponding author: Behrooz Ferdowsi, behrooz@princeton.edu

Abstract

Rate- and State-dependent Friction (RSF) equations are commonly used to describe the time-dependent frictional response of fault gouge to perturbations in sliding velocity. Among the better-known versions are the Aging and Slip laws for the evolution of state. Although the Slip law is more successful, neither can predict all the robust features of lab data. RSF laws are also empirical, and their micromechanical origin is a matter of much debate. Here we use a granular-physics-based model to explore the extent to which RSF behavior, as observed in rock and gouge friction experiments, can be explained by the response of a granular gouge layer with time-independent properties at the contact scale. We examine slip histories for which abundant lab data are available, and find that the granular model (1) mimics the Slip law for those loading protocols where the Slip law accurately models laboratory data (velocity-step and slide-hold tests), and (2) deviates from the Slip law under conditions where the Slip law fails to match laboratory data (the reslide portions of slide-hold-slide tests), in the proper sense to better match those data. The simulations also indicate that state is sometimes decoupled from porosity in a way that is inconsistent with traditional interpretations of “state” in RSF. Finally, if the “granular temperature” of the gouge is suitably normalized by the confining pressure, it produces an estimate of the direct velocity effect (the RSF parameter a) that is consistent with our simulations, and in the ballpark of lab data.

1 Introduction

Models for estimating the length and time scales of earthquake nucleation rely on a mathematical description of the evolution of local fault friction with time (J. H. Dieterich, 1992; J. H. Dieterich & Kilgore, 1996). The commonly accepted framework for modeling this behavior, at least at sliding speeds too small for thermal effects to become important, is “Rate and State-dependent Friction”, or RSF (J. H. Dieterich, 1978, 1979; J. H. Dieterich et al., 1981; A. Ruina, 1983; J. Dieterich, 1994; Marone, 1998b). The RSF framework embodies the notion that frictional strength depends upon a nebulous property termed “state”, a function of recent slip history, as well as the current slip rate. Several versions of rate- and state-dependent friction laws exist, but the two most popular ones are the slip-dependent “Slip law”, which does a better job matching lab data, and the time-dependent “Aging law”, which matches less data (Bhattacharya et al., 2015, 2017), but which has more published theoretical justifications (e.g., Baumberger & Caroli, 2006). However, none of the existing RSF laws reproduce all of the robust features of available laboratory data (Bhattacharya et al., 2017; Kato & Tullis, 2001). This shortcoming, coupled with the largely empirical nature of RSF, severely limits our ability to apply laboratory-derived friction laws to fault slip in the Earth.

In this paper, we adopt the working hypothesis that rock friction is governed by the behavior of a granular gouge with constant Coulomb friction at grain-grain contacts. Note that by not considering time-dependent plasticity or chemical reactions at the contact scale, we are throwing out what is traditionally thought to be the source of the rate- and state-dependence of friction (e.g., J. H. Dieterich & Kilgore, 1994; Baumberger & Caroli, 2006); all the relevant time dependence in our simulations arises from momentum transfer between the gouge particles, even at very low slip speeds. We use the discrete element method to investigate the behavior of a 3-D granular layer sheared at constant normal stress between two rigid and parallel blocks. The model geometry and loading conditions are designed to mimic laboratory rock and gouge friction experiments (we note that laboratory experiments on even initially bare rock surfaces develop, through mechanical wear, either a granular powder or a granular gouge layer, depending upon the total slip distance, and that the phenomenology of RSF is common to both those experiments that start with bare rock and those where gouge is used as the starting material (Marone, 1998b)). In this paper we emphasize velocity-step tests, employing a range of shearing velocities (10^{-5} to 2 m/s) and confining pressures (1 – 25 MPa) to model steps of $\pm 1 - 3$ orders of magnitude. These velocity steps are supplemented by a small number of slide-hold and slide-hold-slide tests designed to allow additional comparisons to laboratory experiments and provide further insight into the gouge behavior.

Consistent with RSF and several earlier numerical studies of sheared granular layers, we find that in response to imposed velocity steps there is an immediate “direct velocity effect” (e.g., an in-

crease in friction in response to a step velocity increase), followed by a more gradual “state evolution effect” where the sign of the friction change is reversed (Morgan, 2004; Hatano, 2009; Abe et al., 2002; Makse et al., 2004). Furthermore, the magnitudes of these direct and evolution effects are proportional to the logarithm of the velocity jump, with implied values of the relevant RSF parameters (a and b) that are not far from lab values.

Perhaps our most significant finding is that the granular flow model mimics the Slip state evolution law for those sliding protocols where the Slip law does a good job matching laboratory experiments, and deviates from the Slip law, in the proper sense to better match lab data, for those sliding protocols where the Slip law does a poor job. The former category includes both velocity-step tests (A. L. Ruina, 1980; A. Ruina, 1983; Tullis & Weeks, 1986; Marone, 1998a; Blanpied et al., 1998; Rathbun & Marone, 2013; Bhattacharya et al., 2015) and slide-hold tests (Bhattacharya et al., 2017). Consistent with both lab experiments and the Slip law, and unlike the Aging law, following a simulated velocity step friction approaches its future steady-state value over slip distances that are independent of both the magnitude and sign of the step (a few grain diameters, in our simulations, or strains of $\sim 15\%$). And consistent with lab experiments, during the hold portion of simulated slide-hold tests stress decays in a manner consistent with the Slip law using RSF parameters not far from those derived from the velocity-step tests, whereas the Aging law, with its time-dependent healing, underestimates the stress decay. Moreover, during the simulated hold the gouge layer compacts roughly as the logarithm of hold time, similar to lab experiments. This is despite the fact that the stress decay, being well-modeled by the Slip law, implies a lack of state evolution. Because state evolution in RSF is traditionally thought to involve the “mushrooming” of contacting asperities and porosity reduction, this indicates that in both the granular simulations and the lab, state is decoupled from gouge thickness (porosity) in a way that is inconsistent with most current interpretations of RSF.

The granular flow model differs from the Slip law prediction during the reslides following holds, in that the Slip law parameters that fit the hold well underestimate the peak stress upon the reslide. Qualitatively, this is the same way in which the Slip law fails to match laboratory data (Bhattacharya et al., 2017). Collectively, our results hint that the physics-based granular flow model may do a better job of matching the transient response of laboratory rock and gouge friction experiments than any existing empirical RSF constitutive law. This is despite having apparently fewer tunable parameters. Although the model contains a large number of dimensionless parameters, most of these are fixed by the boundary conditions and the elastic moduli of the gouge particles, and the remainder seem to exert very little influence on the frictional behavior of the system. An exception is the grain size distribution; we find that a quasi-normal distribution gives rise to steady-state velocity-strengthening behavior, whereas quasi-exponential distribution close to velocity-neutral, perhaps transitioning from velocity-weakening to velocity-strengthening behavior with increasing slip speed. Grain shape may also play a significant role, but only spherical grains are employed here.

The granular model is also well-suited to allowing us to explore the microphysical origins of its RSF-like behavior. In Section 5.4 we begin to address this question, by measuring the kinetic energy of the gouge layer for a range of shear velocities, confining pressures and system sizes. By assuming that this kinetic energy plays the role of temperature in the classical understanding of the rate dependence of friction as a thermally-activated Arrhenius processes (Rice et al., 2001; Lapusta et al., 2000; Chester, 1994; Nakatani, 2001), we obtain an estimate of the magnitude of the direct velocity effect (the RSF parameter a) that is close to that determined by fitting the simulated velocity steps.

In exploring the granular model our intent is not to imply that time-dependent contact-scale processes do not contribute to laboratory friction. Clear evidence of time-dependent contact plasticity comes from the see-through experiments of J. H. Dieterich and Kilgore (1994), and evidence of the importance of chemistry and time-dependent interfacial chemical bond formation comes from, among many other studies, the humidity-controlled gouge experiments of Frye and Marone (2002), and the atomic-force single-asperity slide-hold-slide experiments of Q. Li et al. (2011). It is not yet clear, however, under what conditions such effects dominate the transient frictional strength of

115 interfaces. Nearly all papers that justify a state evolution law on physical grounds do so for the Ag-
 116 ing law (e.g., time-dependent plasticity increasing contact area as log time; Berthoud et al., 1999;
 117 Baumberger & Caroli, 2006), even though this law reproduces relatively little laboratory friction
 118 data. An exception is Sleep (2006), who proposed that the Slip law arises from the highly nonlinear
 119 stress-strain relation at contacting asperities. Here we explore a physics-based model that may do a
 120 better job of matching (room temperature and humidity) laboratory rock and gouge friction data than
 121 any constitutive law currently in use, and that simultaneously allows one to investigate the attributes
 122 of the model that give rise to this behavior.

123 2 Rate- and State-Dependent Friction background

124 Rate- and state-dependent friction laws treat friction as a function of the sliding rate, V , and
 125 the “state variable”, θ . θ has traditionally been thought of as a proxy for true contact area on the
 126 sliding interface (Nakatani, 2001), but it has recently been shown that under some circumstances
 127 time-dependent contact quality can be the dominant contributor to the evolution of state (Q. Li et
 128 al., 2011). In its simplest form, RSF is described by two coupled, first order, ordinary differential
 129 equations. The first describes the relation between friction μ , defined as the ratio of shear stress to
 130 normal stress, and the RSF variables:

$$\mu = \mu_* + a \log \frac{V}{V_*} + b \log \frac{\theta}{\theta_*}, \quad (1)$$

131 where μ_* is the nominal steady-state coefficient of friction at the reference velocity V_* and state θ_* .
 132 The coefficients a and b control the magnitude of velocity- and state-dependence of the frictional
 133 strength, respectively. The second equation describes the evolution of the state variable θ , the two
 134 most widely used forms being

$$\text{Aging Law: } \frac{d\theta}{dt} = 1 - \frac{V\theta}{D_c} \quad (2)$$

$$\text{Slip Law: } \frac{d\theta}{dt} = -\frac{V\theta}{D_c} \ln \frac{V\theta}{D_c} \quad (3)$$

135 with D_c being some characteristic slip distance (J. H. Dieterich, 1979; A. Ruina, 1983). Eq. 2 is
 136 often referred to as the Aging law since state can evolve with time in the absence of slip; Eq. 3 is
 137 referred to as the Slip law since state evolves only with slip ($\dot{\theta} = 0$ when $V = 0$).

138 It is well established that neither the Aging law nor the Slip law adequately describes the full
 139 range of laboratory friction experiments (Beeler et al., 1994; Kato & Tullis, 2001). Laboratory
 140 experiments show that in a sufficiently stiff system, for both initially bare rock samples and gouge,
 141 following a step change in load point velocity friction approaches its new steady-state value quasi-
 142 exponentially over a characteristic slip distance that is independent of both the magnitude and the
 143 sign of the velocity step (A. Ruina, 1983; Marone, 1998b; Blanpied et al., 1998; Bhattacharya
 144 et al., 2015). This is precisely the Slip law prediction of state evolution (Nakatani, 2001). The
 145 Aging law, on the other hand, predicts a slip weakening distance that increases as the logarithm
 146 of the velocity jump for step velocity increases, and, owing to the approximately linear increase
 147 of state with time, exceedingly small slip distances for frictional strength recovery following large
 148 step velocity decreases. Both behaviors are completely inconsistent with laboratory data (Nakatani,
 149 2001).

150 In contrast, conventional wisdom holds that slide-hold-slide experiments are better explained
 151 by the Aging law. In part this stems from the work of Beeler et al. (1994), who ran experiments on
 152 initially bare granite surfaces at two different machine stiffnesses, and hence two different amounts
 153 of slip during the load-point holds. They found that the rate of healing, as inferred from the peak
 154 stress upon the reslide, was independent of stiffness, and hence independent of the small amount of

155 interfacial slip during the load-point holds, seemingly consistent with the Aging law and inconsistent
 156 with the Slip law. However, Bhattacharya et al. (2017) showed that the Beeler et al. peak stress data
 157 could be fit about as well by the Slip law as by the Aging law, and moreover that the stiffness-
 158 dependent stress decay during the load-point holds could be well modeled by the Slip law, although
 159 with a slightly different value of $(a - b)$ than was determined from contemporaneous velocity steps,
 160 and was completely inconsistent with the Aging law. The property of the Aging law that prevents it
 161 from matching the stress decay during the holds is precisely its time-dependent nature: The gouge
 162 strengthens too much to allow any more slip. The rock friction community is thus left in the awkward
 163 position that while most theoretical justifications for state evolution are designed to explain the time-
 164 dependent healing of the Aging law (e.g., Baumberger et al., 1999), this law seems to explain rather
 165 little laboratory rock friction data.

166 3 The computational model

167 Our Discrete Element Method (DEM) simulations are performed using the *granular* module of
 168 LAMMPS (Large scale Atomic/Molecular Massively Parallel Simulator), a multi-scale computational
 169 platform developed and maintained by Sandia National Laboratory ([http://lammps.sandia](http://lammps.sandia.gov)
 170 [.gov](http://lammps.sandia.gov)). What we will refer to as the “default” model consists of a packing of 4815 grains: 4527
 171 in the gouge layer, and 288 in the top and bottom rigid blocks. The grains in the gouge layer have
 172 a polydisperse normal-like size distribution (Figure 1B), with a diameter range $d = [1 : 5]$ mm and
 173 average diameter $D_{mean} = 3$ mm (Figure 1A). The granular gouge is confined between two parallel
 174 and rigid plates that are constructed from grains with diameter $d = 5$ mm. Grain density and Young’s
 175 modulus are chosen equal to properties of glass beads (Table 1). The model domain is rectangular
 176 with periodic boundary conditions applied in the x and y directions. The size of the system in each
 177 direction is $L_x = L_y = 1.5L_z = 20 D_{mean}$.

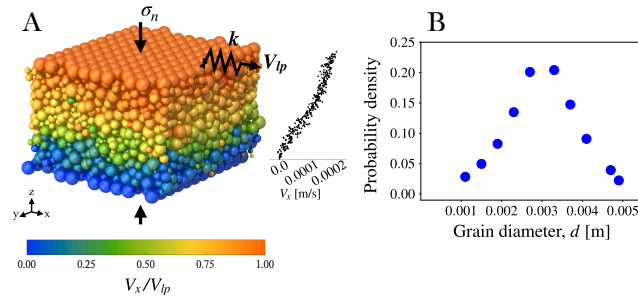


Figure 1. (A) A visualization of the “default” granular gouge simulation. A normal grain size distribution is used, with mean grain diameter $D_{mean} = 3$ mm. Colors show the velocity of each grain in the x direction, averaged over an upper-plate sliding distance of D_{mean} during steady sliding at a driving velocity of $V_{lp} = 2 \times 10^{-4}$ m/s. The actual velocity profile, averaged over 400 planes normal to z , is shown to the right (black dots). (B) The size distribution of grains in the gouge layer in the default model.

178 The system is initially prepared by randomly inserting (under gravity) grains in the simulation
 179 box with a desired initial packing fraction of ~ 0.5 . The system is then allowed to relax for about
 180 10^6 time steps, after which three initially identical and relaxed realizations are subjected to con-
 181 fining pressures $\sigma_n = [1, 5, 25]$ MPa. The confining pressure is applied for one minute, by which
 182 time the fast phase of compaction is completed. These confined gouge samples are then subject
 183 to shearing at a desired driving velocity imposed by the top rigid plate, while the vertical position
 184 of the top wall is adjusted by a servo-control system to maintain the specified (constant) confining
 185 pressure. We find that the servo-control system keeps the normal stress constant to within about
 186 $\pm 0.1\%$ of the desired value at slip speeds of 0.1 m/s (see supplementary Figure S2 for an example
 187 of the servo control during and following a velocity step), and that the variation about the desired

188 value is reduced by about a factor of 5 at slip speeds 5 times smaller. The non-default systems are
 189 prepared using an identical protocol at a confining pressure of $\sigma_n = 5$ MPa. The driving velocity
 190 is applied to the system via a linear spring with a default stiffness of 10^{14} N/m attached to the top
 191 plate; for practical purposes, this stiffness can be considered to be infinite, in that changes in load
 192 point velocity are transferred nearly instantaneously to the upper plate. The grains are modeled
 193 as compressible spheres of diameter d that interact when in contact via the Hertz-Mindlin model
 194 (K. L. Johnson, 1987; Landau & Lifshitz, 1959; Mindlin, 1949).

195 For two contacting particles $\{i, j\}$, at positions $\{\mathbf{r}_i, \mathbf{r}_j\}$, with diameters d_i and d_j , velocities
 196 $\{\mathbf{v}_i, \mathbf{v}_j\}$ and angular velocities $\{\boldsymbol{\omega}_i, \boldsymbol{\omega}_j\}$, the force on particle i is computed as follows: The normal
 197 compression δ_{ij} , relative normal velocity $\mathbf{v}_{n_{ij}}$, and relative tangential velocity $\mathbf{v}_{t_{ij}}$ are given by

$$\delta_{ij} = \frac{1}{2}(d_i + d_j) - r_{ij} \quad (4)$$

$$\mathbf{v}_{n_{ij}} = (\mathbf{v}_{ij} \cdot \mathbf{n}_{ij})\mathbf{n}_{ij} \quad (5)$$

$$\mathbf{v}_{t_{ij}} = \mathbf{v}_{ij} - \mathbf{v}_{n_{ij}} - \frac{1}{2}(\boldsymbol{\omega}_i + \boldsymbol{\omega}_j) \times \mathbf{r}_{ij} \quad (6)$$

198 where $\mathbf{r}_{ij} = \mathbf{r}_i - \mathbf{r}_j$, $\mathbf{n}_{ij} = \mathbf{r}_{ij}/r_{ij}$, with $r_{ij} = |\mathbf{r}_{ij}|$, and $\mathbf{v}_{ij} = \mathbf{v}_i - \mathbf{v}_j$. The rate of change of the elastic
 199 tangential displacement $\mathbf{u}_{t_{ij}}$, set to zero at the initiation of a contact, is given by

$$\frac{d\mathbf{u}_{t_{ij}}}{dt} = \mathbf{v}_{t_{ij}} - \frac{(\mathbf{u}_{t_{ij}} \cdot \mathbf{v}_{ij})}{r_{ij}^2} \quad (7)$$

200 where the second term in equation 7 comes from the rigid body rotation around the contact point.
 201 Its implementation is there to insure that $\mathbf{u}_{t_{ij}}$ always locates in the local tangent plane of contact
 202 (Silbert et al., 2001). The normal and tangential forces acting on particle i are then given by:

$$\mathbf{F}_{n_{ij}} = \sqrt{\delta_{ij}} \sqrt{\frac{d_i d_j}{2(d_i + d_j)}} (k_n \delta_{ij} \mathbf{n}_{ij} - m_{eff} \gamma_n \mathbf{v}_{n_{ij}}) \quad (8)$$

$$\mathbf{F}_{t_{ij}} = \sqrt{\delta_{ij}} \sqrt{\frac{d_i d_j}{2(d_i + d_j)}} (-k_t \mathbf{u}_{t_{ij}} - m_{eff} \gamma_t \mathbf{v}_{t_{ij}}) \quad (9)$$

203 where k_n and k_t are the normal and tangential stiffness, given by $k_n = (2/3)E/(1 - \nu^2)$ and $k_t =$
 204 $2E/(1 + \nu)(2 - \nu)$ (Mindlin, 1949), with E being Young's modulus and ν Poisson's ratio, and $m_{eff} =$
 205 $m_i m_j / (m_i + m_j)$ is the effective mass of spheres with masses m_i and m_j (we note that the most
 206 appropriate value of k_t seems to be a matter of some debate, with Schäfer et al. (1996) suggesting
 207 values roughly 1000 times smaller). γ_n and γ_t are the normal and tangential damping (viscoelastic)
 208 constants, respectively; we maintain the default LAMMPS option of $\gamma_t = 0.5\gamma_n$. As indicated by
 209 equations 8 and 9, the model implements damping for both normal and tangential contacts as a
 210 spring and dashpot in parallel. Note that the Hertzian normal force given by (8) increases non-
 211 linearly with grain compression δ_{ij} (equation 4), as $\delta_{ij}^{3/2}$ in the absence of damping, consistent with
 212 the elastic deformation of contacting spheres.

213 In a gravitational field \mathbf{g} , the translational and rotational accelerations of particles are deter-
 214 mined by Newton's second law, in terms of the total forces and torques on each particle, i :

$$\mathbf{F}_i^{tot} = m_i \mathbf{g} + \sum_j (\mathbf{F}_{n_{ij}} + \mathbf{F}_{t_{ij}}) \quad (10)$$

$$\boldsymbol{\tau}_i^{tot} = -\frac{1}{2} \sum_j \mathbf{F}_{t_{ij}} \times \mathbf{r}_{ij} \quad (11)$$

215 The grain-grain coefficient of friction, μ_g , is the upper limit of the tangential force through the
 216 Coulomb criterion $F_t \leq \mu_g F_n$. The tangential force between two grains grows according to the
 217 non-linear Hertz-Mindlin contact law until $F_t/F_n = \mu_g$ and is then held at $F_t = \mu_g F_n$ until either
 218 $F_t \leq \mu_g F_n$ or the grains loose contact.

The amount of energy lost in collisions is characterized by the coefficient of restitution. The values of restitution coefficients, ϵ_n and ϵ_t for the normal and tangential directions respectively, are related to their respective damping coefficients $\gamma_{n,t}$ and contact stiffness $k_{n,t}$. The restitution coefficient for the normal direction can be calculated by solving the following equation that describes the normal component of the relative motion of two spheres in contact:

$$\ddot{\delta} + \frac{E\sqrt{2d_{eff}}}{3m_{eff}(1-\nu^2)} \left(\delta^{3/2} + \frac{3}{2} A \sqrt{\delta} \dot{\delta} \right) = 0 \quad (12)$$

219 with the initial conditions $\dot{\delta}(0) = v_n$ and $\delta(0) = 0$. In this equation, $A = \frac{1}{3} \frac{(3\gamma_t - \gamma_n)^2}{(3\gamma_t + 2\gamma_n)} \left(\frac{(1-\nu^2)(1-2\nu)}{E\nu^2} \right)$,
 220 and $d_{eff} = d_i d_j / (d_i + d_j)$ is the effective diameter for spheres of diameters d_i and d_j . The normal
 221 component of the coefficient of restitution can be obtained from the ratio of normal velocity of grains
 222 at the end of the collision, defined as $\dot{\delta}(t_{col})$, to their initial normal impact velocity: $\epsilon_n = \dot{\delta}(t_{col})/\dot{\delta}(0)$.
 223 The collision time t_{col} is determined by solving Eq. 12 for the adopted physical properties and initial
 224 velocities of two colliding grains. A similar procedure is performed for calculating the restitution
 225 coefficient in the tangential direction. We use a time step of $\Delta t = t_{col}/100$ throughout this study,
 226 with t_{col} evaluated assuming an impact velocity $\dot{\delta}(0)$ of 25 m/s (t_{col} in (12) depends very weakly
 227 upon $\dot{\delta}(0)$, as roughly $\dot{\delta}(0)^{1/5}$ (Shäfer et al., 1996)). The restitution coefficient in the default model
 228 is chosen to be very high ($\epsilon_n = 0.98$), such that the system is damped minimally. Although in one
 229 sense damping introduces time-dependence at the contact scale, we find by varying the restitution
 230 coefficients from nearly zero (complete damping) to nearly 1 (no damping) that they exert no sig-
 231 nificant influence on the system behavior in the slow-sliding regime of interest. For this reason we
 232 refer to the model as having no time-dependence at the contact scale. The full details of the granular
 233 module of LAMMPS are described in the LAMMPS manual and several references (Zhang & Makse,
 234 2005; Silbert et al., 2001; Brilliantov et al., 1996).

235 In addition to the default model, we have run simulations with a domain size twice the size
 236 of the default model, simulations with a grain and domain size two orders of magnitude smaller,
 237 simulations with grain-grain friction coefficients of 1.0 and 5.0 (default = 0.5), simulations with
 238 restitution coefficients ϵ_n of 0.003 to 0.82 (default = 0.98), and simulations with either a quasi-
 239 exponential grain size distribution. The influence of most of these changes on the model results are
 240 rather modest, and we relegate detailed figures to the supplementary materials of this manuscript. An
 241 exception are the models with a different grain size distribution; these are described in section 5.2.6.
 242 A full accounting of the dimensionless parameters governing the model is provided in Appendix A.
 243 In principle, we wanted to prepare models that could isolate the influence of each parameter that we
 244 tested. However, because of the way we used the LAMMPS random particle generator, in some cases
 245 there are slight variations in the total number of particles, which are reflected in different values of
 246 L_z (hereafter referred to as the gouge thickness H). Compared to the default model, for the simu-
 247 lations with different grain-grain friction coefficients H is larger by 10%; for the simulations with
 248 a grain and domain size two orders of magnitude smaller the ratio H/D_{mean} is larger by 7%, and
 249 in the simulations where L_x and L_y are two times larger, H is only 1.8 times larger (we continue to
 250 refer to this as the “two-times larger” model).
 251

252 Table 1. DEM simulation parameters. The “default model” values, where multiple values are
 253 given, are in bold font.

Parameter	Value
Grain density, ρ	2500 [kg/m ³]
Young’s modulus, E	50 [GPa]
Poisson ratio, ν	0.3
254 Grain-grain friction coefficient, μ_g	0.5 , 1.0, 5.0
Confining pressure, σ_n	1, 5 , 25 [MPa]
Coefficient of restitution, ϵ_n	0.98 , 0.82, 0.25, 0.01, 0.003
Time step, Δt	2×10^{-8} [s]

255 The velocity V in the RSF equations (1)–(3) is interpreted in laboratory experiments as the
 256 inelastic component of the relative tangential displacement rate between two parallel planes. This
 257 displacement rate is typically treated conceptually as occurring across a plane of zero thickness,
 258 but in fact it occurs across a zone whose thickness is generally unknown. In lab experiments, the
 259 relative displacement is measured between two points outside the zone of inelastic deformation, and
 260 the inelastic component of that displacement δ is determined by subtracting the estimated elastic
 261 displacement δ_{el} from the measured (total) displacement, i.e.

$$\begin{aligned}\delta &= \delta_{lp} - \delta_{el} = \delta_{lp} - \tau/k, \\ \tau &= k(\delta_{lp} - \delta),\end{aligned}\tag{13}$$

262 where δ_{lp} is the measured “load-point” displacement (in our simulations the displacement of the
 263 end of the spring not attached to the upper plate), τ the spring force divided by the nominal sample
 264 surface area (6 cm \times 6 cm in our default model), and k the elastic stiffness of the combined testing
 265 apparatus plus sample between the measurement points. In our numerical simulations this stiffness
 266 is given by the effective stiffness of two springs in series,

$$k_{\text{eff}} = \frac{k_{sp}k_H}{k_{sp} + k_H},\tag{14}$$

267 where k_{sp} and k_H are the spring and gouge stiffness, respectively. To measure k_H , we performed
 268 several slide-hold-reslide simulations with a range of hold durations (Figure B1). The shear modu-
 269 lus can be estimated from the initially linear (assumed to be elastic) portion of the reslide following
 270 the longest holds in such simulations (e.g., Bhattacharya et al., 2017). From these tests, the shear
 271 modulus of the gouge layer is estimated to be in the range of $G_H \approx 270$ to 310 MPa, at a confining
 272 pressure of 5 MPa. This estimate is about 30 – 50% lower than previous experimental measure-
 273 ments on granular layers made from packing glass beads (Yin, 1993; Domenico, 1977; Makse et
 274 al., 1999), and granular simulations with properties similar to our model. However, those previ-
 275 ous experiments and simulations were performed under specially designed preparation protocols, to
 276 produce a maximal packing fraction under a given confinement. We expect our simulation samples
 277 (that are generated under conditions similar to synthetic gouge experiments) to have a lower pack-
 278 ing fraction and to exhibit a lower shear modulus. Although the appropriate value of G_H may vary
 279 modestly with the sliding history and packing properties of the gouge, we neglect this possibility
 280 here. For G_H from 270 to 310 MPa, the stiffness k_H varies from $G_H/H = 6.75 \times 10^9$ to 7.75×10^9
 281 Pa/m, where $H = 0.04$ m is the gouge thickness. To determine k_{sp} in Pa/m from the stiffness input
 282 in LAMMPS in units of N/m, we divide by the sample surface area. For the default spring stiffness
 283 of 10^{14} N/m, $k_{sp} \sim 3 \times 10^{16}$ Pa/m $\gg k_H$, so $k_{\text{eff}} \sim k_H$. This value of k_{eff} is so large that even
 284 large errors in G_H play no role in the Slip law fits to our simulated velocity steps (k_{eff} is essentially
 285 infinite).

286 Using (13) and (14) ensures that our analysis is consistent with both the conventional inter-
 287 pretation of equations (1)–(3) and standard laboratory protocols. For example, with k_{sp} essentially

288 infinite and V_{Ip} set to zero (a “hold”), the upper plate remains stationary, but due to granular rear-
 289 rangements within the gouge the inelastic displacement δ increases and $V > 0$ as the stress relaxes.

290 4 Previous studies of granular rheology related to rock friction

The granular model has many dimensionless parameters, but most turn out to be unimportant in the region of parameter space of interest (Appendix A). Within the physics literature, the most important is understood to be the Inertial number, defined as

$$I_n \equiv \dot{\gamma} D_{mean} \sqrt{\rho/P} \approx \frac{V}{H} D_{mean} \sqrt{\rho/P}, \quad (15)$$

291 where $\dot{\gamma}$ is the local shear rate (approximated as the slip speed divided by the gouge thickness
 292 in the second expression), P is the confining pressure (or normal stress, for the geometry of our
 293 simulations), and ρ and D_{mean} are the density and mean diameter of grains, respectively. The inertial
 294 number measures the ratio of the inertial forces of grains to the confining forces acting on those
 295 grains, such that small values ($I_n \lesssim 10^{-3}$) correspond to the quasi-static state. A continuum model
 296 that has proven moderately successful in modeling steady-state granular friction is known as $\mu(I_n)$
 297 rheology (Forterre & Pouliquen, 2008), where the local coefficient of friction depends only upon
 298 the local inertial number. However, in some regions of parameter space the dimensionless pressure,
 299 defined as $\bar{P}_{Hertz} \equiv (P/E)^{2/3}$ for the Hertzian contact law that we use, and as $\bar{P}_{Hook} \equiv PD_{mean}/k_{grain}$
 300 for a linear ($F_n \propto \delta_{ij}$) Hookean contact law (appropriate for 2-D simulations, with k_{grain} being the
 301 adopted grain-grain spring stiffness), also plays a role. Both versions of \bar{P} are proportional to the
 302 nominal elastic strain of grains subjected the applied load, given the adopted contact law (Salerno
 303 et al., 2018; DeGiuli & Wyart, 2017), and we only distinguish between them when necessary. For
 304 granular gouge with a quartz-like modulus ($E \sim 50$ to 70 GPa) and normal stresses from 2 to 50
 305 MPa, \bar{P}_{Hertz} varies from $\sim 10^{-3}$ to 10^{-2} ; the “rigid grain” (undeforming) limit is thought to be
 306 reached in the limit $\bar{P} \lesssim 10^{-3}$ (DeGiuli & Wyart, 2017; de Coulomb et al., 2017).

307 The steady-state behavior of sheared granular layers has been studied extensively in the past
 308 two decades, using both simulations and experiments. Most numerical studies have explored values
 309 of I_n from roughly 10^{-5} to 10^0 , crossing the quasi-static to inertial transition. These studies gener-
 310 ally find steady-state friction to be well fit by a power-law of the form $\mu_{ss} = \mu_0 + b I_n^\alpha$, with μ_0 , b and
 311 α being fitting parameters. When plotted vs $\log(I_n)$ or $\log(V)$, friction is strongly velocity(rate)-
 312 strengthening within the inertial regime, transitioning to weakly velocity-strengthening and ulti-
 313 mately asymptoting to velocity-neutral with decreasing I_n within the quasi-static regime (da Cruz et
 314 al., 2005; de Coulomb et al., 2017; Kamrin & Koval, 2014; Hatano, 2007). In contrast, some labora-
 315 tory studies of sheared granular flow find velocity-weakening behavior within the quasi-static regime
 316 (Dijksman et al., 2011; Kuwano et al., 2013; G. H. Wortel et al., 2014), but potentially this could be
 317 due to time-dependent contact-scale processes not accounted for in the numerical simulations. How-
 318 ever, in a theoretical study DeGiuli and Wyart (2017) concluded that a sheared 2-D granular layer
 319 with a Hookean contact law changes behavior from velocity-strengthening for $I_n \gtrsim 10^{-3}$ to slightly
 320 velocity-weakening at lower I_n , asymptoting to velocity-neutral as I_n decreases further, provided
 321 $\bar{P} \lesssim 10^{-3}$.

322 Studies of granular gouge layers away from steady state are much less common and are mostly
 323 restricted to the geological literature. Using a model of a sheared granular fault gouge, Morgan
 324 (2004) observed both the direct and state evolution effects in velocity-stepping tests, and the logarithmic-
 325 with-time healing of friction upon resliding in slide-hold-slide tests. In those simulations Morgan
 326 introduced a time-dependent grain-grain contact law, with $\mu_g \propto \log[\text{contact time}]$. Likewise, Abe et
 327 al. (2002) implemented the Slip law version of state evolution to describe the time-dependence of the
 328 grain-grain friction coefficient in slide-hold-slide simulations, and again observed logarithmic heal-
 329 ing of friction with time upon resliding. Because both of these studies introduced time-dependence
 330 at the contact scale, it is difficult to isolate the purely geometrical contribution of granular flow to
 331 the transient frictional behavior they observed. Furthermore, neither study compared their results to
 332 laboratory experiments at the level of detail required, for example, to distinguish between competing
 333 state evolution laws. Hatano (2009) simulated velocity-stepping experiments, in 3 dimensions but

334 using a linear (Hookean) contact law for grain-grain interactions, for a range of inertial numbers
 335 $10^{-5} \lesssim I_n \lesssim 10$, and dimensionless pressures $10^{-5} \lesssim \bar{P} \lesssim 10^{-1}$. He observed a critical slip dis-
 336 tance that scaled linearly with the size of the velocity steps, behavior that is not reproduced by our
 337 simulations and that is also inconsistent with laboratory rock friction experiments.

338 In the RSF framework, a steady-state velocity-weakening system and a system stiffness be-
 339 low a critical value are necessary conditions for stick-slip motion. Using a very soft spring for
 340 applying the sliding velocity ($k_{\text{spring}} \sim 3 \times 10^{-5} k_{\text{grain}}$, where k_{grain} is grain stiffness), Aharonov and
 341 Sparks (2004) performed DEM simulations of a two dimensional confined sheared granular layer
 342 for $6 \times 10^{-4} \lesssim I_n \lesssim 0.2$ and $10^{-5} \lesssim \bar{P} \lesssim 10^{-3}$. They showed that the frictional behavior changes
 343 from stick-slip to oscillatory motion to steady-sliding as I_n increases. Similar behavior was later re-
 344 produced by Ferdowsi et al. (2013). Neither Aharonov and Sparks (2004) nor Ferdowsi et al. (2013)
 345 directly measured the steady-state friction coefficient as a function of velocity, so it is not clear if
 346 their systems were in the rate-weakening regime when stick-slip behavior emerged, or whether in
 347 granular systems stick-slip may occur despite the system being rate-strengthening. One could imag-
 348 ine, for example, that with a sufficiently soft spring and a system small enough for only a small
 349 number of force chains to develop, collapse of a force chain might lead to sudden accelerations. The
 350 existence, origins and controls of a transition from rate-weakening to rate-strengthening behavior
 351 in sheared granular layers is still a matter of much debate (Perrin et al., 2019; van Hecke, 2015).
 352 Recent experimental and numerical studies show that the variation of friction coefficient with shear
 353 rate and inertial number depends on the grain shape, surface roughness, and size distribution (Mair
 354 et al., 2002; Salerno et al., 2018; Murphy, Dahmen, & Jaeger, 2019; Murphy, MacKeith, et al.,
 355 2019). In our preliminary results examining the influence of grain size distribution, we find that the
 356 behavior changes from velocity strengthening to approximately velocity neutral when the grain size
 357 distribution is changed from quasi-normal to quasi-exponential.

358 A continuum model for the flow of amorphous materials, recently applied to granular gouge,
 359 is known as Shear Transformation Zone (STZ) theory (Lemaître, 2002; Manning et al., 2007). In
 360 response to imposed velocity steps, STZ models exhibit both a direct velocity effect and an opposing
 361 state evolution effect, consistent with lab experiments and RSF (Daub & Carlson, 2008; Lieou et
 362 al., 2017). However, STZ models have yet to be compared to lab data at the level of, for example,
 363 establishing the basic result that the slip distance for stress (or state) evolution following an imposed
 364 velocity step is independent of the magnitude and sign of that step (Bhattacharya et al., 2015). Such
 365 tests matter because, as stated previously, simply documenting that a model has a direct and an
 366 evolution effect is insufficient justification for applying it to processes such as earthquake nucleation
 367 (Ampuero & Rubin, 2008). Furthermore, in the most recent versions of STZ (Lieou et al., 2017; Ma
 368 & Elbanna, 2018), variations in the state variable (“compactivity”) are assumed to be proportional
 369 to the gouge volume (thickness) change. However, both our granular simulations and laboratory
 370 friction experiments (to be discussed in section 5.2), and recent granular physics studies (Bililign
 371 et al., 2019; Puckett & Daniels, 2013) indicate that gouge thickness change is an inadequate description
 372 of state. Continuum approaches such as STZ theory may benefit from detailed studies of the granular
 373 physics of RSF of the sort described in this manuscript.

374 5 Results

375 5.1 Steady-state friction

376 The results of granular simulations run to quasi-steady-state at different normal stresses and
 377 driving velocities are shown in Figure 2. Because individual runs tend to be somewhat noisy, pre-
 378 sumably due to the relatively small system size, each data point is averaged over seven different
 379 realizations (initial packings) of the granular fault gouge, and each of these realizations is averaged
 380 over a sliding distance of five times the mean grain diameter D_{mean} . Friction in this and all figures in
 381 this paper is defined as the ratio of shear to normal stress τ/σ , with τ and σ defined as the shear and
 382 normal force per unit area exerted by the gouge particles on the upper (driving) plate. This definition
 383 ensures that we are measuring the frictional strength of the gouge at the boundary with the upper
 384 plate, should that differ from the applied spring force (any mismatch leading to acceleration of the

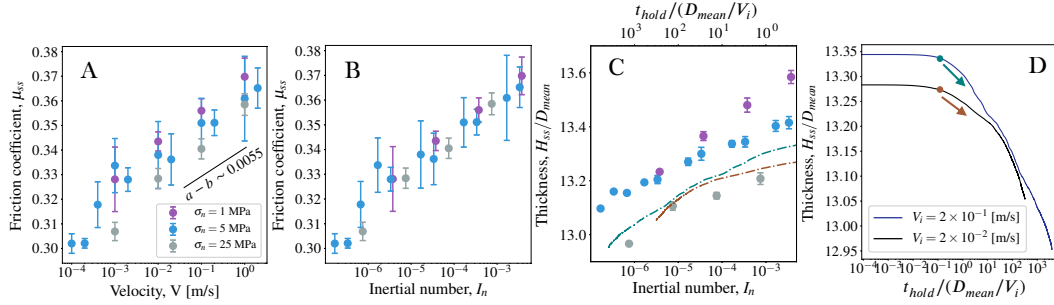


Figure 2. (A) The variation of steady-state friction coefficient with driving velocity at three different normal stresses. (B) The same data plotted as a function of inertial number (I_n). (C) The variation of steady-state gouge thickness at different driving velocities as a function of I_n , for the same three normal stresses. Error bars indicate one standard deviation of all friction measurements over a sliding distance of $5D_{mean}$ for each of the seven different realizations (initial grain arrangements) at each normal stress and V_{Ip} . Most error bars in (C) are smaller than the symbol size. The dashed teal and brown lines in (C) show the temporal evolution (upper horizontal axis) of gouge thickness in the hold experiments shown in panel (D). (D) The evolution of gouge thickness with time during slide-hold experiments at $V_i = 2 \times 10^{-1}$ and 2×10^{-2} m/s. Zero time in these plots marks the start of the hold (the halting of the upper driving plate). The teal and brown dots and arrows show the starting point and temporal progression of the curves that we plot in panel (C) (time progresses to the left in C). The confining pressure is $\sigma_n = 5$ MPa.

385 upper plate). In the absence of significant accelerations that are coherent when averaged over $x - y$
 386 planes, from force balance the shear stress as we have defined it is uniform throughout the gouge.

387 The nominal friction coefficient in Figure 2A, ~ 0.33 , is low by laboratory standards. This
 388 low value is likely due to the use of spherical grains, as laboratory studies also show mean nomi-
 389 nal friction coefficients in the range 0.25 – 0.45 for glass beads and for synthetic gouge layers
 390 produced from spherical grains (Anthony & Marone, 2005). Mair et al. (2002) also found that by
 391 changing grain shapes from smooth spherical to angular the mean steady-state friction increases
 392 from ~ 0.45 to ~ 0.6 . A recent computational study by Salerno et al. (2018) further shows that using
 393 non-spherical grains shifts the dynamic friction versus inertial number curves upward uniformly,
 394 increasing mean friction values from 0.25 – 0.35 for spheres to the 0.5 – 0.6 range for rounded-edge
 395 cubic grains. Note that for comparison to RSF we are primarily concerned with the variations of
 396 friction with slip rate and slip history. In the absence of thermal weakening mechanisms, numerical
 397 simulations of fault slip in an elastic solid depend only upon the time-variation of friction and not
 398 its absolute value.

399 For our default model we find steady-state friction to vary essentially linearly with the logarithm
 400 of slip speed over the full range of parameters we have explored. Such behavior has been previously
 401 observed in solid-on-solid friction in many different materials (Baumberger et al., 1999; Berthoud et
 402 al., 1999; J. H. Dieterich, 1979; A. Ruina, 1983; Karner & Marone, 1998), as well as in experiments
 403 with spherical and non-spherical granular particles at low inertial numbers (Hartley & Behringer,
 404 2003; Behringer et al., 2008) [although it is arguable that in experiments, time-dependent contact-
 405 scale processes may contribute to the observed logarithmic rate-dependence (Heslot et al., 1994;
 406 Nakatani, 2001)]. We find velocity-strengthening behavior over the range of parameters explored
 407 thus far, consistent with many experiments on gouge, although many other gouge experiments show
 408 nearly velocity-neutral behavior (Marone, 1998b; Marone et al., 1990). The value of $|a - b|$ from the
 409 slope of our data, ~ 0.0055 , is slightly high by lab standards, but Marone et al. (1990) found values
 410 as high as 0.005 for laboratory gouge, and we emphasize that unlike standard RSF and STZ theory
 411 this value is an output of the model and not a tunable parameter.

412 Note that in Figure 2A the friction coefficient increases slightly with decreasing normal stress.
 413 This is not a feature of standard RSF, but it is consistent with some laboratory data (e.g., J. H. Di-
 414 eterich, 1972). If the data are plotted against the inertial number I_n rather than velocity (Figure 2B),
 415 there is a near collapse of all observations onto a single curve, as expected from previous work. Rel-
 416 ative to previous numerical studies we explore a somewhat lower range of I_n (roughly $10^{-7} - 10^{-2}$,
 417 compared to $10^{-5} - 10^0$). While those previous studies found steady-state friction to have a power-
 418 law dependence upon I_n , they are nonetheless consistent with ours in that for the overlapping range
 419 of I_n ($\sim 10^{-5} - 10^{-2}$) they can be fit quite well by a logarithmic dependence of friction upon I_n ,
 420 with a slope not much different than ours (Hatano, 2007). It is within the inertial regime of flow,
 421 for $I_n \gtrsim 10^{-2}$, that the steady-state friction vs. $\log(I_n)$ curves in previous studies become strongly
 422 concave-up and require a power-law fit. Our steady-state results differ from previous simulations
 423 mostly in extending the range of I_n lower by ~ 2 orders of magnitude, the lowest we can achieve in
 424 a few weeks of computation time. We find the logarithmic dependence to continue to those lower
 425 values, while the power-law fits adopted by previous studies continue to flatten with decreasing I_n
 426 (for further discussion see supplementary information Section 1 and supplementary Figure S1).

427 To estimate how our range of I_n compares to that accessed by typical laboratory gouge friction
 428 experiments, we note with reference to equation (15) that such experiments typically don't vary
 429 very far from our value of $(\rho/P)^{1/2}$. This means that if our adopted value of $D_{mean}/H \sim 1/13$ is
 430 appropriate, our simulations will have basically the same I_n as a lab experiment with the same V .
 431 The synthetic gouge experiments of Mair and Marone (1999), for example, spanned slip speeds of
 432 $0.3-3000 \mu\text{m/s}$, compared to our lowest V of $200 \mu\text{m/s}$. Thus, typical low-velocity lab friction
 433 experiments can be expected to overlap the lowest values of I_n we explore, but to extend to values
 434 of I_n several orders of magnitude lower still. At slip speeds within the upper half of our range,
 435 say 0.1 m/s , thermal weakening mechanisms are expected to dominate over classical RSF in rock
 436 friction experiments (e.g., Rice, 2006). To estimate I_n for the Mair and Marone (1999) experiments
 437 more precisely we can use their $P = 25 \text{ MPa}$ and initial value of $D_{mean}/H \approx 1/30$ (initial grain size
 438 $50-150 \mu\text{m}$; gouge thickness 3 mm), to obtain $10^{-10} < I_n < 10^{-6}$. For experiments accompanied
 439 by grain comminution and strain localization over a thickness H_{eff} , I_n will vary to the extent that
 440 D_{mean}/H_{eff} varies from $\sim 1/30$ (although the behavior at a given I_n could change for non-spherical
 441 particles, and if the grain size distribution becomes very large then the appropriate choice of D_{mean}
 442 in the definition of I_n might need to be re-examined). Based upon experimental studies summarized
 443 by Rice (2006), shear bands in granular sands with a relatively narrow size distribution often satisfy
 444 $D_{mean}/H_{eff} \sim 1/10 - 1/20$.

445 The steady-state gouge thickness H in our simulations decreases with increasing normal stress,
 446 but increases quasi-linearly with $\log(I_n)$ at a rate that is only weakly dependent on normal stress
 447 (Figure 2C). The logarithmic rate-dependence of gouge thickness, with the gouge thickness change
 448 ΔH being $\sim 0.1 D_{mean}$ per order of magnitude increase in driving velocity, also seems roughly
 449 consistent with laboratory observations (Rathbun & Marone, 2013; Beeler & Tullis, 1997; Marone
 450 & Kilgore, 1993). (We show in the next section that in our simulations $0.1 D_{mean} \sim 0.05 D_c$, which
 451 enables a comparison with lab experiments where D_c is estimated but not D_{mean} .)

452 The temporal evolution of the gouge layer thickness in two slide-hold simulations is shown
 453 in semi-log scale in Figure 2D. Both the friction coefficient (shown later in Figure 12A) and the
 454 gouge thickness show a relaxation with the logarithm of time. We compare the compaction rate of
 455 the gouge during the holds to the dilation rate as a function of inertial number in Figure 2C. The
 456 similar slopes of the thickness data from the steady-sliding experiments (dots) and the holds (teal
 457 and brown lines) show that the reduction in gouge thickness that results from a ten-fold increase
 458 in hold duration is comparable to the reduction from a ten-fold decrease in inertial number (\sim slip
 459 speed). This suggests that the origin of the velocity-dependence of steady-state gouge thickness may
 460 lie in the same slow relaxation process that operates during holds. J. H. Dieterich (1978) proposed
 461 a somewhat analogous equivalency between increased hold duration and decreased slip speed in
 462 laboratory experiments: That contact strength increased logarithmically with age, whether that age
 463 was defined as the duration of a hold, or as the typical contact lifetime (contact dimension divided
 464 by the steady sliding speed).

465

5.2 Velocity step simulations

466

467

468

469

470

471

472

473

474

475

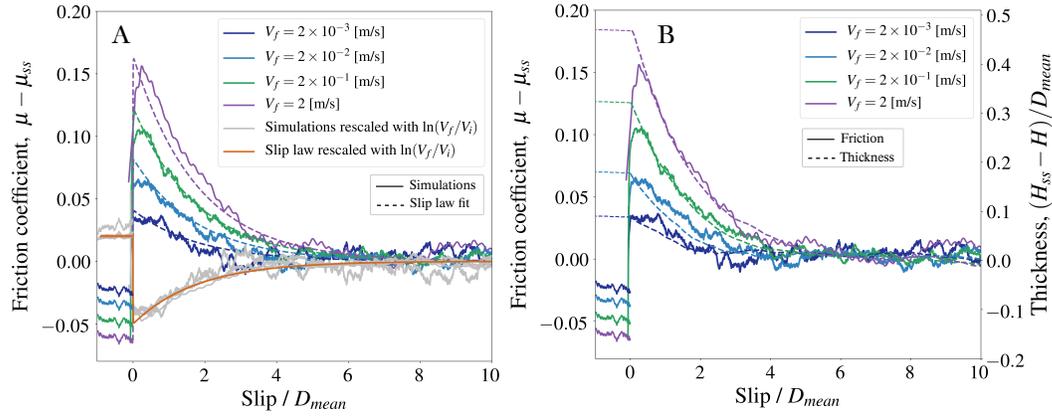


Figure 3. (A) Results from step velocity increases with initial load-point velocity $V_i = 2 \times 10^{-4}$ m/s. The friction coefficient, plotted relative to its future steady state value to emphasize the state evolution, is shown as a function of shear slip distance normalized by D_{mean} . Slip in this and later figures is defined to be zero at the time of the step. The curve for the 4-order increase to $V_f = 2$ m/s jumps discontinuously backward to a small negative slip value because equation (13) does not account for elastodynamic effects (see Appendix B). The gray curves are the friction signals rescaled as $-0.05(\mu - \mu_{ss})/b \ln(V_f/V_i)$ (the -0.05 is used just to make all signals visible on the same axis). The dashed lines show the prediction of the Slip law with $b = 0.0178$, $a = 0.0247$ and $D_c = 1.78D_{mean}$ (see text). (B) The solid lines show the variation of friction with normalized slip from panel (A). The dashed lines show the difference between the steady-state gouge thickness H_{ss} and the current thickness H , normalized by the mean grain diameter D_{mean} (the gouge dilates with slip). The results are averaged over seven different realizations of the same imposed loading conditions, with σ_n fixed at 5 MPa.

476

477

478

479

480

481

482

483

484

485

486

487

Given the increase in steady-state gouge thickness with slip speed/inertial number (Figure 2C), it seems reasonable to suggest that the direct velocity effect comes from sliding at the new (higher) slip speed but with the old (compacted) gouge thickness, while the state evolution effect is associated with the gradual approach to the new steady-state gouge thickness. A direct correspondence between state and gouge porosity has also been proposed in the context of both RSF (Segall & Rice, 1995; Sleep, 2006) and STZ theory (Lieou et al., 2017). However, although this view has some intuitive appeal, we show below that it is too simplistic; there is not a one-to-one relation between “state” and gouge thickness. (We also note here, in anticipation of results to be presented in section 5.2.2, that in simulations that use the same particle size distribution but a gouge thickness H 1.8 times larger, the gouge evolves to steady state over a slip distance roughly 1.8 times larger; that is, state evolution seems to be governed by a critical strain rather than by a critical slip distance. For convenience, we speak here of a critical slip distance. This does not alter our previous estimate of $\Delta H/D_c$ for a given

488 log velocity change, where ΔH is the change in gouge thickness, because in our simulations both
 489 ΔH and D_c are proportional to H .)

490 The gray curves in Figure 3A show these friction changes normalized by the logarithm of the
 491 velocity jump, and are flipped for ease of visualization. That the gray curves all nearly overlap,
 492 that is, have approximately the same scaled amplitude and approach the new steady state over the
 493 same sliding distance, is entirely consistent with the Slip law description of state evolution with
 494 quasi-constant values of a , b , and D_c (Bhattacharya et al., 2015). Using a simplex method we find
 495 the single set of (Slip law) RSF parameters that best matches these velocity jumps to be $a \sim 0.025$,
 496 $b \sim 0.018$, and $D_c \sim 1.8D_{mean}$. These values of a and b are on the high side but are within a factor
 497 of 2 of those commonly cited for rock and gouge, and we again emphasize that they are an output
 498 of the model and not an input. The dashed curves in Figure 3A show the Slip law predictions for
 499 these velocity steps, using these parameter values. The Slip law predicts the behavior of the granular
 500 model quite well, excluding the initial rounding that occurs over a slip distance of up to $\sim D_{mean}$ in
 501 the simulations. For the 4-order velocity jump to 2 m/s there is some contribution to the measured
 502 shear stress from bulk inertia of the gouge; however, this contribution is expected to be small for
 503 slip distances larger than a modest fraction of D_{mean} , and should not influence the Slip law fit to the
 504 data (Appendix B).

505 Figure 3B shows the variation of gouge thickness with slip distance (dashed lines) in compar-
 506 ison to the variation of friction coefficient, for the same velocity steps in panel A. The simulations
 507 show that the gouge layer approaches its future steady state thickness H_{ss} over a slip distance com-
 508 parable to the slip distance for the evolution of friction (the gouge dilates with slip, but we plot
 509 $H_{ss} - H$ for easier comparison to the friction data). The good correlation between gouge thickness
 510 and friction (and hence $\log[\text{state}]$), and the accepted parallels between state and gouge thickness
 511 (i.e., that the mushrooming of asperities that increases contact area also brings the surfaces closer
 512 together (Sleep, 1997)), make it natural to ask whether variations in gouge thickness are a useful
 513 proxy for variations in state.

514 Figure 4A shows results for similar simulations with an initial steady-state load-point velocity
 515 of 10^{-2} m/s, and velocity steps of up to +2 and -3 orders of magnitude. These show that friction
 516 evolves to its new steady state over a slip distance that is independent of the sign as well as the mag-
 517 nitude of the velocity step, again precisely the Slip-law description of state evolution. The variation
 518 of gouge thickness during these velocity steps is shown in Figure 4B, which indicates that the gouge
 519 thickness for velocity step increases evolves to its new steady state over a slip distance comparable to
 520 that for the evolution of stress, as in Figure 3B. In contrast, the gouge thickness during velocity step
 521 decreases evolves to its new steady state over a slip distance shorter than that observed for the fric-
 522 tion coefficient in the same experiments, especially for the two- and three-order-of-magnitude step
 523 downs. This is emphasized by the gray curves in Figure 4B, which show the thickness evolution for
 524 the step velocity decreases, flipped and rescaled to cover the same range as the corresponding 1- and
 525 2-order step increases (the total thickness change is larger for the step increases). This asymmetry
 526 of the transient response to changes in driving velocity, in conjunction with the symmetric response
 527 of the friction coefficient, indicates that gouge thickness is an incomplete description of state. Other
 528 aspects of the granular structure, such as force fabric and structural anisotropy, must contribute to
 529 the state of the system.

530 The prediction that gouge thickness evolves much more rapidly with slip in response to step
 531 velocity decreases than increases appears to be borne out by laboratory experiments (Figure 4C; see
 532 also Rathbun and Marone (2013, Figures 6-7) and Mair and Marone (1999, Figure 10a)), although
 533 a more systematic comparison to existing lab data is certainly warranted. In fact, the asymmetric
 534 response of the gouge thickness in the simulations is very reminiscent of the Aging law prediction
 535 for friction, especially the modified form of the Aging law that T. Li and Rubin (2017) argued was
 536 more faithful to the underlying concept of contact “age” (their Figure 5a). We will return to this
 537 point during the discussion of slide-hold simulations.

538 The single set of (Slip law) RSF parameters that best matches the velocity steps with $V_i = 10^{-2}$
 539 m/s are determined from the simplex method to be $a = 0.024$, $b = 0.018$, and $D_c = 1.7D_{mean}$, very

540 similar to the values determined previously for the step increases from $V_i = 2 \times 10^{-4}$ m/s. Laboratory
 541 investigations of the velocity-dependence of the RSF parameters show somewhat mixed results. For
 542 order-of-magnitude velocity steps on initially bare granite samples, B. D. Kilgore et al. (1993) found
 543 variations of a and b of no more than a few tens of percent for initial velocities ranging over 4 orders
 544 of magnitude. In contrast, similar experimental protocols conducted by Mair and Marone (1999)
 545 on synthetic fault gouge indicate that D_c increases systematically by up to 2 orders of magnitude,
 546 and that (for sample slip distances exceeding ~ 15 mm) a decreases systematically by a factor of
 547 2–3, as the initial velocity increases over a range of 3 orders of magnitude. However, using similar
 548 starting materials, Bhattacharya et al. (2015) found that velocity step increases of 1 and 2 orders of
 549 magnitude from a single starting velocity, and step decreases of 1 and 2 orders of magnitude back to
 550 that same velocity, were fit extremely well by the Slip law with constant RSF parameters.

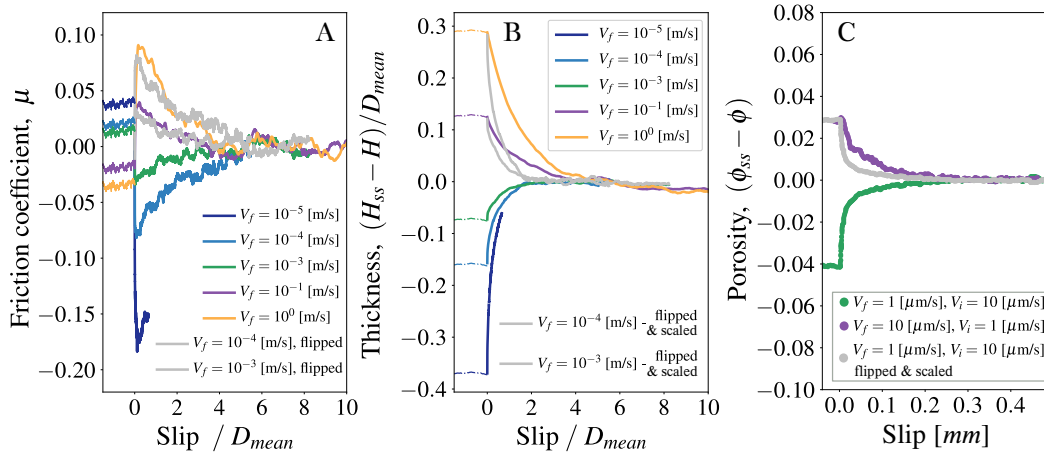


Figure 4. The variation of (A) friction coefficient and (B) gouge thickness, in simulations with velocity steps up to +2 and –3 orders of magnitude. The initial driving velocity in all tests is $V_i = 10^{-2}$ m/s. The simulation with $V_f = 10^{-5}$ m/s has yet to run to completion (the future steady state values are estimates only), but is sufficient to demonstrate that the thickness initially varies much more rapidly than stress. The gray curves in (A) are the step-down simulations, flipped to emphasize the stress symmetry between the step increases and decreases. The results in both panels are averaged over seven different realizations, with normal stress fixed at 5 MPa. (C) The variation of porosity in gouge experiments in response to ± 1 order of magnitude increases and decreases in velocity from and back to the initial velocity of $V = 1 \mu\text{m/s}$. The experiments were performed by Marone et al. (1990, as reported by Segall and Rice, 1995) on water saturated but drained (\sim constant pore pressure) layers of Ottawa sand. The gray curves in panels (B) and (C) are step-down simulations (B) and the lab experiment (C), flipped and scaled to the same initial value as the corresponding step up, to emphasize the much more rapid response (with respect to slip) of porosity (thickness) to the velocity step decreases.

5.2.1 The influence of confining pressure

551

552 In addition to velocity steps at a normal stress of $\sigma_n = 5$ MPa and initial velocities V_i of 10^{-2}
 553 and 2×10^{-4} m/s, we also conducted 1- to 3-order-of-magnitude velocity increases at $\sigma_n = 1, 5$ and
 554 25 MPa at $V_i = 10^{-3}$ m/s. The results, shown in Figure 5, indicate that the magnitude of direct and
 555 evolution effects vary slightly but not systematically with σ_n . We again search for the single sets
 556 of (Slip law) parameters that best match all the velocity jumps at each confining pressure, using the
 557 simplex method (Table 2). Except for D_c being modestly larger at the largest σ_n , and a and b being
 558 larger at the smallest σ_n , the parameters seem to be largely independent of confining pressure.
 559

559

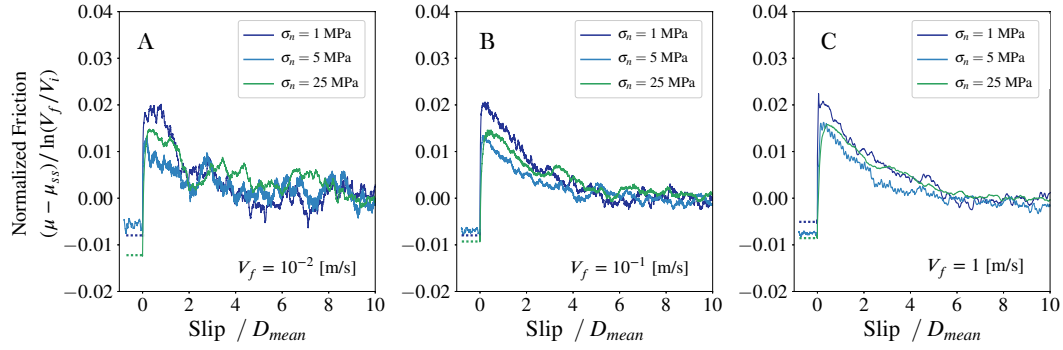


Figure 5. The variation of normalized friction coefficient, $(\mu - \mu_{ss})/\ln(V_f/V_i)$, for velocity step-ups of (A) one order, (B) two orders, and (C) three orders of magnitude, in systems with confining pressure $\sigma_n = 1, 5,$ and 25 MPa. With this normalization, rough estimates of a (the jump across the velocity step) and b (the amplitude of the decay following the peak) can be read directly from the vertical scale (the signal/noise ratio increases with the size of the velocity step). The initial driving velocity is $V_i = 10^{-3}$ m/s in all tests. The results are averaged over seven different realizations of the same imposed loading conditions.

560 Table 2. The RSF parameters obtained for velocity steps at $\sigma_n = 1, 5$ and 25 MPa and $V_i =$
 561 10^{-3} m/s.

Normal stress σ_n	RSF parameters			
	a	b	$a - b$	D_c/D_{mean}
1 MPa	0.0290	0.0226	0.0064	1.83
5 MPa	0.0202	0.0135	0.0067	1.92
25 MPa	0.0232	0.0145	0.0087	3.23

562

563 5.2.2 Critical slip distance or critical strain?

564 The critical slip distance in our default system velocity-step experiments is roughly 1.7 times
 565 the mean particle diameter D_{mean} (see Figs. 3-4). This seems reasonable, given that in laboratory
 566 fault friction experiments the critical slip distance D_c is often interpreted as being close to an
 567 asperity size (Marone, 1998b; J. H. Dieterich et al., 1981). However, laboratory data are somewhat
 568 ambiguous with regard to whether a critical strain or a critical slip distance controls the approach
 569 to a new frictional equilibrium. J. H. Dieterich et al. (1981) reported that the critical slip distance
 570 is largely independent of gouge thickness, an observation he interpreted as indicative of slip local-
 571 ization within the gouge (i.e., a critical strain over a layer thickness that was insensitive to gouge
 572 thickness). Marone and Kilgore (1993) reported that some gouges had a critical slip distance that
 573 increased quasi-linearly with gouge thickness (i.e., a critical strain), while others had a much weaker
 574 dependence upon thickness, possibly reflecting variable degrees of localization.

575 We have run step velocity increase simulations from $V_i = 10^{-2}$ m/s using the model that has
 576 twice the dimensions of the default model (although 1.8 times the thickness), with all other grain
 577 and system properties being identical to the default model. A comparison to the default model is
 578 shown in Figure 6. We find that the critical slip distance following velocity steps is 1.9 times as
 579 long in simulations with 1.8 times the model thickness (RSF parameters: $a = 0.028$, $b = 0.019$, and
 580 $D_c/D_{mean} = 3.3$, compared to $a = 0.024$, $b = 0.018$, and $D_c/D_{mean} = 1.7$ for the default model at
 581 $V_i = 10^{-2}$ m/s), suggesting that indeed it is a critical strain that governs the approach to the new
 582 steady state. As a result, rescaling the slip distance (x-axis) by the ratio of the model dimensions

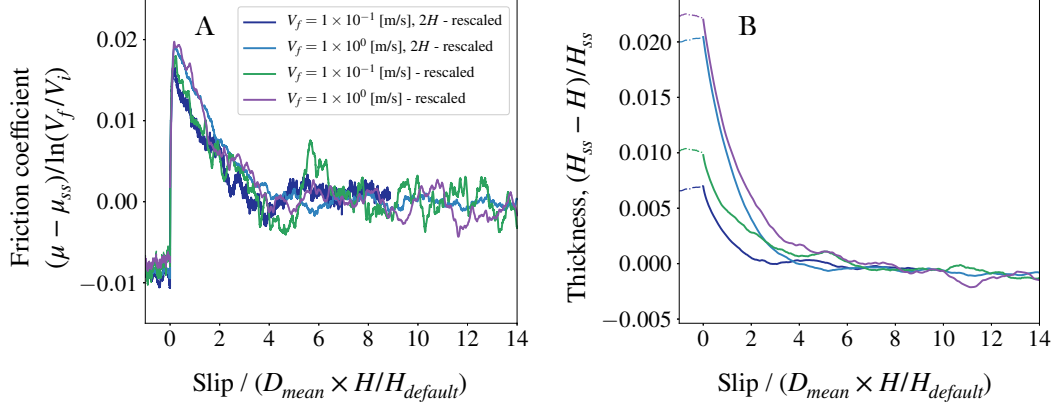


Figure 6. (A) The variation of normalized friction coefficient with normalized slip for velocity step-ups of 1–2 orders of magnitude, in the default system and the system with twice the domain size. (B) The variation of the gouge thickness normalized by the initial gouge thickness for the same velocity steps in (A). In both panels, the slip distance (x-axis) is scaled by the ratio of the gouge thickness to the default gouge thickness H_{default} . $V_i = 10^{-2}$ m/s and $\sigma_n = 5$ MPa. The results are averaged over seven different realizations of the same imposed loading conditions.

583 shows that the frictional behavior for both systems almost collapses (with some noise) to a single
 584 curve. The critical strain, using $\gamma_{xz} = \partial u_x/\partial z + \partial u_z/\partial x = \partial u_x/\partial z$, is $\gamma_{xz_c} \sim D_c/H \sim 0.13$. In
 585 contrast, the gouge thickness curves, when normalized by their (future) steady-state values, do not
 586 completely collapse when plotted as a function of rescaled slip distance (Figure 6B). We obtained
 587 similar results (not shown here) for $V_i = 10^{-1}$ and 10^{-3} m/s.

588 5.2.3 The gouge dilation angle

589 Several authors have commented on the potentially important contribution of fault gouge di-
 590 latancy or compaction to the measured value of friction (Morrow & Byerlee, 1989; Morgan, 2004;
 591 Marone et al., 1990; Beeler & Tullis, 1997). Marone et al. (1990) proposed that the “apparent”
 592 friction, μ^A , defined as the ratio of the shear to normal stress τ/σ (what is measured in laboratory
 593 experiments and our numerical simulations), can be written

$$\frac{\tau}{\sigma} = \mu^A = \mu^f + \frac{d\delta_n}{d\delta_s}, \quad (16)$$

594 where $d\delta_n/d\delta_s$ is the instantaneous ratio of fault-normal displacement δ_n to slip δ_s (dilation taken
 595 to be positive and compaction negative here), and μ^f can be considered to be some hypothetical
 596 “intrinsic” friction that would be measured in the absence of fault-normal displacements.

597 Changes in $d\delta_n/d\delta_s$ in lab experiments are often larger than changes in the observed friction
 598 μ^A . Because of this, Beeler and Tullis (1997) pointed out that if μ^f is thought to be given by
 599 equation (1), the direct effect parameter a would have to be negative; i.e., at constant state, materials
 600 would have to weaken with increasing slip speed. As this violates standard interpretations of the
 601 source of the direct effect, they argued that μ^f should be interpreted not as resulting from the total
 602 energy dissipated in the fault zone, but as only the energy dissipated in fault-parallel shear. They
 603 showed that with this definition of μ^f , the time-dependent plastic contribution to $d\delta_n/d\delta_s$ should be
 604 neglected in equation (16).

605 For granular models we are not persuaded that it is useful to speak of an “intrinsic” friction
 606 that is distinct from the contribution of dilatancy to the measured μ^A . And, as a practical matter, it

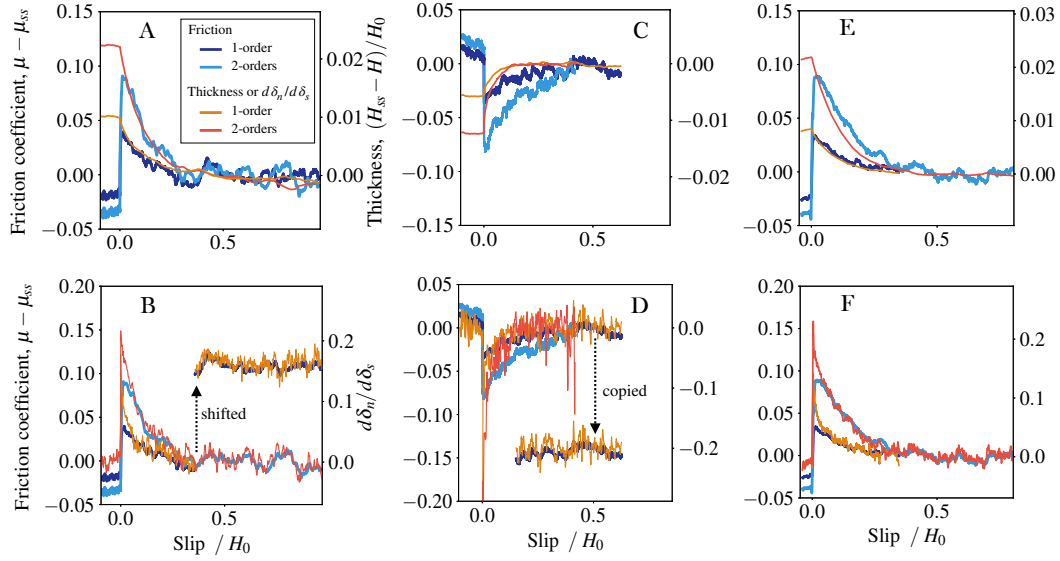


Figure 7. (A-C-E) The variation of frictional resistance and normalized gouge thickness with slip distance in velocity step tests. Slip here is normalized by the nominal gouge thickness H_0 , so the horizontal axis is the nominal shear strain. (A): The default model with step increases of 1 and 2 orders of magnitude. (C): The default model with step decreases of 1 and 2 orders of magnitude. (E): Step increases of 1 and 2 orders of magnitude in the system with twice the dimensions of the default model. The thickness change in these panels is normalized by H_0 , so the vertical axis is the nominal dilational strain, but the scale factor relating the normalized thickness and friction axes in each panel is the same as in Figure 4. (D-B-F) The variation of friction and normal to shear deformation rate with respect to normalized slip distance for the same experiments shown in the panels immediately above. The ratio between the $d\delta_n/d\delta_s$ and friction scales (1.44) is the same in all panels. The $d\delta_n/d\delta_s$ minima in panel (D) are at -0.25 and -1.38 (the latter off scale) for the 1- and 2-order step decreases, respectively. All experiments are performed at $\sigma_n = 5$ MPa and $V_i = 10^{-2}$ m/s; H_0 is taken to be the value of H_{ss} under these conditions. The results are averaged over seven different realizations of the same imposed loading conditions.

607 is not trivial to separate $d\delta_n/d\delta_s$ as observed in laboratory experiments into time-dependent plastic
 608 and slip-dependent geometric components, as advocated by Beeler and Tullis (1997). Nonetheless,
 609 our measurements of $d\delta_n/d\delta_s$ can be compared to both laboratory experiments and our measured
 610 μ^A . Figure 7 shows the evolution of friction, the gouge layer thickness, and $d\delta_n/d\delta_s$, for 1- and
 611 2-order-of-magnitude velocity step increases and decreases for our default model, as well as 1- and
 612 2-order-of-magnitude step increases for the model with dimensions twice as large. The scale factor
 613 between friction and thickness changes in panels A, C, and E is the same as in Figures 3, 4, and
 614 6. As in those figures, there is a reasonably close correlation between the measured friction and
 615 gouge thickness for the step increases but not the step decreases. However, the correlation between
 616 the measured friction and $d\delta_n/d\delta_s$ for the step increases, as well as for the step decreases once the
 617 system is close to steady state, is even more striking. Note the difference in scale; the variation in
 618 $d\delta_n/d\delta_s$ is about 40–50% larger than the variation in μ^A . In steady-sliding laboratory experiments
 619 on 2-D glass rods, Frye and Marone (2002) found a ratio closer to 1. Hazzard and Mair (2003)
 620 also found a ratio of ~ 1 at steady state for both 2-D and 3-D granular simulations with Hertzian
 621 grain-grain interactions.

622 Our granular simulations show that upon a step increase in velocity, the maximum value of
 623 $d\delta_n/d\delta_s$ exceeds the direct-effect friction change $\Delta\mu_{\text{direct}}$ by anywhere from a few tens of percent
 624 to a factor of about two (Figures 7B and 7F). The difference is larger in our simulated velocity-step

625 decreases; because of the more rapid evolution of thickness with slip, $d\delta_n/d\delta_s$ following the velocity
 626 step exceeds $\Delta\mu_{\text{direct}}$ by more than a factor of 5 for the 1-order step down and more than a factor of
 627 10 for the 2-order step down (Figure 7D). These results are within the ballpark of laboratory values.
 628 In experiments on synthetic gouge in a triaxial shear apparatus, Marone et al. (1990, figures 20-21)
 629 find that $d\delta_n/d\delta_s$ exceeds $\Delta\mu_{\text{direct}}$ by a factor of 4–6, independent of the magnitude of the velocity
 630 step, for both step increases and the one step decrease shown. Using data from the same paper,
 631 however, and plotting thickness as a function of slip, Segall and Rice (1995) show an example
 632 (reproduced here as Figure 4C) for which $d\delta_n/d\delta_s$ is significantly larger for the step down than
 633 the step up. Similarly, Mair and Marone (1999, figure 10a) show thickness vs. slip for a 1-order
 634 velocity step increase and decrease in a double-direct shear experiment on synthetic gouge where
 635 $(d\delta_n/d\delta_s)/\Delta\mu_{\text{direct}}$ is about 2.5 for the step increase, but many times larger for the step decrease
 636 (for the step increase $(d\delta_n/d\delta_s)/\Delta\mu_{\text{direct}} \sim 0.03/0.005 \ln[10]$, where 0.005 is the value of a for
 637 $\sigma_n = 25$ MPa, total slip 18–20 mm, and $V = 1$ to 10 mm/s in their figure 8a). Using a rotary
 638 shear apparatus, Beeler and Tullis (1997) present data from 1-order velocity step decreases where
 639 $d\delta_n/d\delta_s$ exceeds $\Delta\mu_{\text{direct}}$ by a few tens of percent for initially intact granite that develops a gouge
 640 layer through wear, and by a factor of about 2.5 for synthetic granite gouge. This is an area where a
 641 more thorough comparison between the granular gouge simulations and existing laboratory data is
 642 certainly warranted.

643 As a final investigation of equation (16), we ran velocity-step simulations while enforcing a
 644 constant volume (gouge thickness) boundary condition ($d\delta_n/d\delta_s = 0$, so $\mu^A = \mu^f$). For a step
 645 increase this entails a transient increase in normal stress, as the gouge, which dilates at constant normal
 646 stress, is prevented from doing so. Remarkably, the transient friction response in the constant-
 647 volume simulations is indistinguishable from that in the corresponding constant-normal-stress simu-
 648 lations (Figure 8). We are thus faced with the surprising observation that at constant normal stress
 649 there is a very close correlation between $d\delta_n/d\delta_s$ and μ^A for most of the friction evolution after the
 650 step velocity increases in Figs. 7B and 7F, seemingly consistent with the spirit of equation (16),
 651 while essentially identical friction evolution occurs in simulations in which $d\delta_n/d\delta_s$ is forced to be
 652 zero.

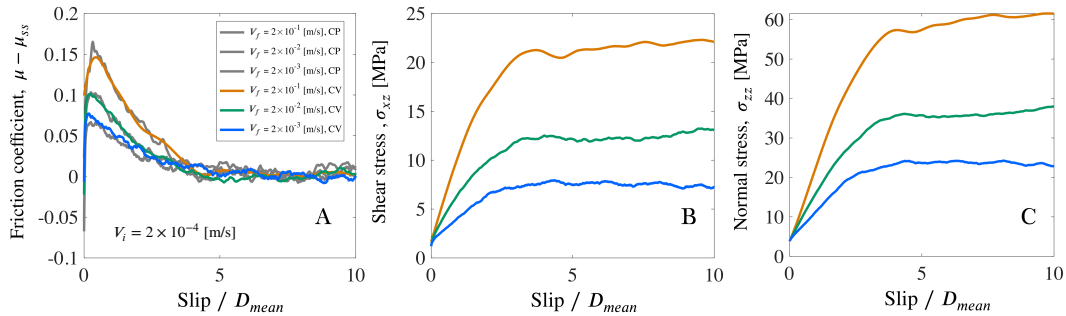


Figure 8. Results from constant-volume velocity-step experiments. (A) shows the variation of friction; (B) and (C) show the variation of shear and normal stress applied by gouge grains to the driving plate, as functions of slip distance. All experiments use the default model with an initial normal stress of 5 MPa and $V_i = 2 \times 10^{-4}$ m/s. Gray lines in (A) show the frictional behavior for the corresponding constant normal stress experiments. The results are averaged over seven different realizations of the same imposed sliding conditions.

653 5.2.4 Is there localization in the granular gouge layer?

654 A plot of the particle velocity through the gouge, $u_x(z)$, spatially averaged over x and y and
 655 temporally averaged over an upper plate displacement of $0.1D_{\text{mean}}$, is shown in Figure 9A for a
 656 steady-state shearing simulation performed at the load-point velocity $V_{lp} = 10^{-2}$ m/s. The steady-
 657 sliding velocity profile decays linearly away from the shearing plate, and shows no sign of localiza-

658 tion. Following an order of magnitude velocity-step increase, we further measure the velocity vari-
 659 ation with distance from the driving plate during the first $0.001 D_{mean}$, $0.01 D_{mean}$ and $0.1 D_{mean}$
 660 shearing distance. The results are plotted in Figures 9B-D and show no signs of strain localization
 661 immediately or shortly after the velocity step (in Figure 9B the shear wave generated by the velocity
 662 step at the upper plate has yet to reach the bottom plate; see Appendix B). Hatano (2015) suggested
 663 that the duration of the friction transient following his simulated velocity steps might correspond to
 664 the slip distance required for the gouge to approach its new steady state velocity profile, but as this
 665 occurs over distances $< 0.1 D_{mean}$ in Figure 9, compared to slip distances of several D_{mean} for the
 666 friction transient, this is clearly not the case in our simulations.

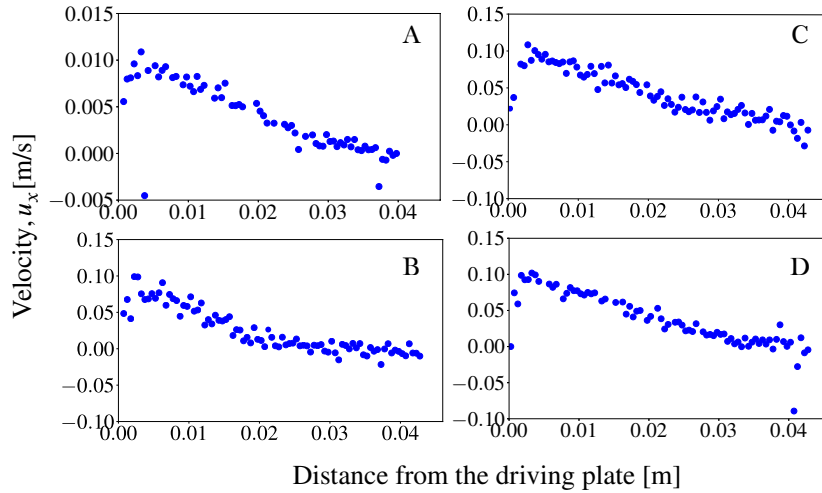


Figure 9. The velocity profile of the granular gouge in the default system. The driving velocity is initially $V_i = 10^{-2}$ m/s, as in Figure 4. Panel (A) shows the velocity profile at steady sliding with velocity V_i , measured over a slip distance $0.1 D_{mean}$. Panels (B), (C) and (D) show the velocity profiles measured in the first $0.001 D_{mean}$, $0.01 D_{mean}$, and $0.1 D_{mean}$, respectively, following an order of magnitude step velocity increase. In (B), the shear wave generated by the velocity jump at the upper plate just 3×10^{-5} s earlier has traversed only about half the gouge thickness (see Appendix B). The normal stress is fixed at 5 MPa. The indicated velocity is a spatial average over the x and y directions.

667 The absence of localization in our system is also consistent with the adopted dimensionless
 668 pressure ($\bar{P}_{\text{Hertz}} = [P/E]^{2/3} \sim 2 \times 10^{-3}$ for $\sigma_n = 5$ MPa), which puts it near the stiff or rigid grain
 669 limit. The studies by de Coulomb et al. (2017) and Bouzid et al. (2015) show that in our range
 670 of packing pressure and inertial numbers, systems do not show persistent localized deformation,
 671 although Aharonov and Sparks (2002) report periods of spontaneous transient slip localization in
 672 2-D simulations with $\bar{P}_{\text{Hook}} = 10^{-3}$. In contrast, persistent patterns of localized deformation in
 673 the form of simple shear bands are expected in systems that operate in the soft grain regime ($\bar{P} \gg$
 674 10^{-3}) (de Coulomb et al., 2017; Le Bouil et al., 2014; Amon et al., 2012; Darnige et al., 2011).
 675 In laboratory experiments on synthetic gouge (Sleep et al., 2000), and gouge formed by wear of
 676 initially intact rock (Beeler et al., 1996), slip appears to be localized, but this may be associated
 677 with processes such as grain breakage that are not included in our model (see Abe and Mair (2009)
 678 for a granular simulation that includes grain breakage at the grain scale, and Aghababaei et al. (2018) for
 679 atomistic simulations that include asperity breakage and wear at the atomic scale).

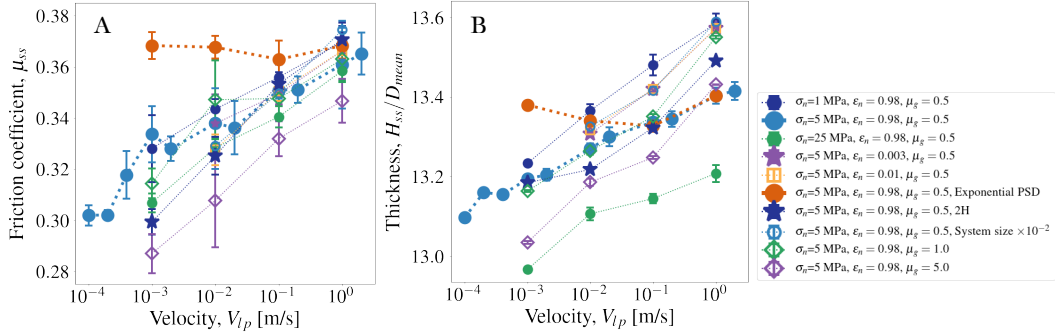


Figure 10. (A) The variation of steady-state friction coefficient with driving velocity in the default system at three different normal stresses, and in systems with different values of the grain-grain friction coefficient, restitution coefficient, size (smaller by 100x), ratio of steady-state gouge thickness H_{ss} to mean particle diameter D_{mean} ($1.8\times$ larger), and grain size distribution (quasi-exponential). (B) The variation of H_{ss}/D_{mean} for the simulations in (A). For models that have a different number of grains per unit area ($L_x \times L_y$) than the default model, the ratio H_{ss}/D_{mean} has been further normalized by the ratio of that number to the number of grains per unit area in the default model (a correction that is $\leq 10\%$ for the models with the same L_x and L_y). This normalization is performed for the systems with quasi-exponential grain size distribution, with 1.8 times the H_{ss}/D_{mean} of the default model (2H), and with different restitution coefficients and grain-grain friction coefficients. Error bars indicate one standard deviation of all friction measurements over a sliding distance of $5D$ for each of seven different realizations (initial grain arrangements). Most error bars in (B) are smaller than the symbol size.

5.2.5 The influences of grain-grain friction coefficient, restitution coefficient, and grain size

To explore the generality of our observations and which grain-scale properties may influence the results, we investigated the steady-state behavior, and the transient response to velocity-steps, of systems with different grain-grain friction coefficients, grain-grain restitution coefficients, and (while keeping the ratio of gouge thickness to grain size fixed) grain size. Figure 10 shows the variation of the steady-state friction coefficient (A) and gouge thickness (B) with driving velocity for the default system and for systems with different grain properties. The variation of steady-state friction with driving velocity is somewhat sensitive to the details of the system, although frictional behavior remains velocity-strengthening for all cases with mean slopes of $0.005 \leq (a - b) \leq 0.007$. The variation of gouge thickness with velocity shows that the gouge layer remains logarithmically dilatant, with similar normalized dilation rates of roughly $0.01D_{mean}$ per decade, corresponding to normal strains of order 10^{-3} per decade, for all systems.

Note that increasing the grain-grain friction coefficient decreases the macroscopic friction slightly, consistent with previous studies (Silbert, 2010), presumably as a result of enhanced grain rolling. From dimensional analysis, decreasing the grain and system sizes by the same scale factor is not expected to lead to differences in macroscopic behavior, as this changes only the magnitude of the gravitational stress relative to the confining pressure, which is already extremely low (Appendix A). Comparing the default model to the system reduced in scale by a factor of 100 in Figure 10 shows that this is generally the case, to within the scatter of the data.

The choice of restitution coefficient ϵ also has very little influence on frictional behavior. Figure 10A shows that values of ϵ_n ranging from nearly fully damped (0.003 and 0.01) to near-zero damping (the default value of 0.98) show essentially the same value of μ_{ss} as a function of velocity. Previous numerical studies have also demonstrated that for inertial numbers $I_n \lesssim 10^{-2}$, varying the grain-grain damping exerts almost no influence on the steady-state frictional behavior of the system

705 (MiDi, 2004) (this is unlike the behavior at higher I_n , where increasing the damping during grain-
 706 grain collisions decreases the rate of velocity strengthening and dilation with increasing driving
 707 velocity and inertial number (Silbert et al., 2001; MiDi, 2004)).

708 The influence of these grain-scale properties on the transient frictional response to velocity-
 709 step tests were also very modest. Although we have not formally fit the results to determine the RSF
 710 parameters a , b , and D_c , directly comparing the transient responses to those for the default model
 711 generally show differences that are within or near the apparent noise level (Supplementary Figures
 712 S3, S5, and S6).

713 5.2.6 The influence of grain size distribution

714 Unlike the grain-scale properties of the previous section, we find that grain size distribution
 715 has a dramatic influence on the macroscopic behavior of the system. We have run simulations with
 716 a quasi-exponential grain size distribution, which better represents actual fault gouge (Marone &
 717 Scholz, 1989; Sammis & King, 2007; Billi, 2005; An & Sammis, 1994). For the quasi-exponential
 718 size distribution, we targeted generating a distribution with grain sizes ranging from 0.5 to 5 mm,
 719 with $D_{mean} = 1.5$ mm, and distribution form $PDF(D) = \lambda^{-1} \exp[-(D - \mathcal{M})/\lambda]$, with distribution
 720 parameters $\mathcal{M} = 1$ mm and $\lambda = 2$ mm. The resulting system, generated by a random particle gener-
 721 ation algorithm in LAMMPS, has $D_{min} = 0.5$ mm, $D_{max} = 4.9$ mm, and $D_{mean} = 1.5$ mm. We
 722 reduced D_{mean} by half, relative to the default system, to ensure that the largest particle size was no
 723 larger than the 5-mm particles in the bounding rigid blocks (larger gouge particles led to a roughly
 724 5-mm periodicity in friction during quasi-steady sliding). We also found that the exponential dis-
 725 tribution led to apparently noisier (more variable) friction during steady sliding; on the assumption
 726 that a longer model dimension in the sliding direction would reduce the influence of individual force
 727 chains, the quasi-exponential system was given dimensions $L_x = 4L_y = 6L_z = 160 D_{mean}$ (Figure
 728 11). This reduced the apparent noise substantially. A few simulations of the same dimension using
 729 the quasi-normal grain size distribution verified that increasing L_x/L_z from 1.5 to 6.0 didn't change
 730 the steady-state friction level, its dependence upon slip speed, the rate of change of gouge thickness
 731 with shear velocity, or the qualitative behavior of the system during velocity-stepping or slide-hold
 732 protocols.

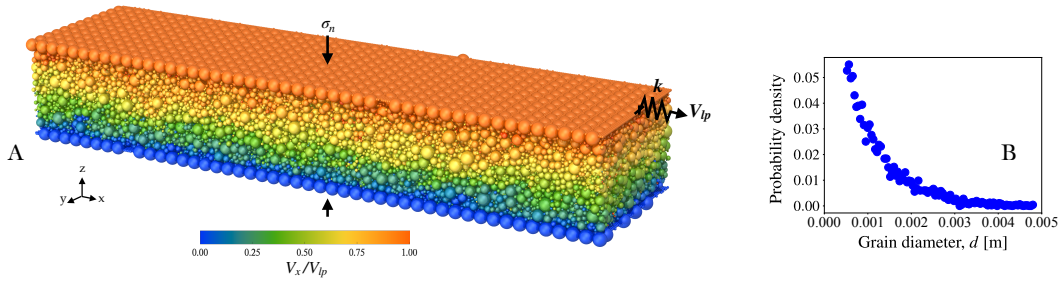


Figure 11. (A) Visualization of the virtual rock gouge experiment with the quasi-exponential grain size distribution, with mean grain diameter $D_{mean} = 1.5$ mm. Colors show the velocity of each grain in the x direction, averaged over an upper-plate sliding distance of D_{mean} . The driving velocity is $V_{ip} = 0.1$ m/s. (B) The size distribution of grains in the gouge layer.

733 The variation, with driving velocity, of the steady-state friction coefficient and gouge thick-
 734 ness for the quasi-exponential grain size distribution are shown by the solid orange symbols in
 735 Figs. 10A and B, respectively. Given the error bars in panel A, one could perhaps argue that
 736 the system is velocity-neutral. However, because the gouge thickness, which has much smaller un-
 737 certainties, decreases as V_{ip} increases from 10^{-3} to 10^{-1} m/s, and increases from 10^{-1} to 1 m/s, we
 738 think it is more likely that the system is steady-state velocity strengthening as the shear velocity
 739 increases from $V_{ip} = 10^{-1}$ to 1 m/s, and nearly velocity-neutral or slightly velocity-weakening as

740 V_{lp} increases from 10^{-3} to 10^{-1} m/s (an association between steady-state velocity-weakening and
 741 gouge-thinning, and steady-state velocity-strengthening and gouge-thickening, underlies recent ver-
 742 sions of STZ theory (Lieou et al., 2017)). Therefore the gouge thickness, and perhaps the friction
 743 coefficient, vary non-monotonically with driving velocity. DeGiuli and Wyart (2017) previously
 744 observed a non-monotonic variation of friction coefficient with shear velocity in 2-D granular sim-
 745 ulations and in the range of \bar{P} and inertial numbers we have explored. The grain size distribution
 746 used in their model is not specified. The non-monotonic variation of friction coefficient has also
 747 been observed in several experimental granular physics studies, including those by Dijkstra et al.
 748 (2011), G. H. Wortel et al. (2014), and G. Wortel et al. (2016). However, it is not straightforward
 749 to separate the potential contributions of time-dependent contact-scale processes from purely gran-
 750 ular rearrangements in those experiments. van der Elst et al. (2012) also observed a non-monotonic
 751 variation of gouge thickness with shear rate in experiments using angular grain shapes, while exper-
 752 iments using spherical grains showed a monotonic increase of gouge thickness with shear rate. The
 753 friction coefficient, and the influence of grain size distribution on the velocity-dependence of gouge
 754 thickness, were not explored in their study.

755 We also performed a limited number of velocity-step simulations using the quasi-exponential
 756 grain size distribution. The results are shown in Supplementary Figure S7. They include a subset of
 757 1- and 2-order-of-magnitude velocity steps up or down from initial driving velocities of 10^{-2} , 10^{-1} ,
 758 and 1 m/s. Owing to the large model size we averaged only 3 realizations of each set of conditions,
 759 and the results are much noisier than for our normal distribution simulations (although less noisy
 760 than the average of 7 realizations of the exponential distribution using the default simulation size).
 761 All of these tests show a direct velocity effect and an opposing state evolution effect, with $a \sim 0.0085$
 762 for the step with the highest signal/noise ratio (a 2-order step down; Supplementary Figure S7-C),
 763 and values not far from this for the others. This is within the range typically reported for laboratory
 764 experiments (e.g., Mair & Marone, 1999).

765 The variation of gouge thickness following step velocity changes between 0.1 and 1 m/s, where
 766 steady-state friction and gouge thickness increase with slip speed, is similar to the behavior of mod-
 767 els with a quasi-normal grain size distribution, in that the thickness monotonically approaches its
 768 future steady-state value at a decaying rate. However, for steps between velocities in the range of
 769 10^{-3} to 10^{-1} m/s, where steady-state thickness (and perhaps friction) decrease with increasing slip
 770 speed, the transient thickness change becomes nonmonotonic. Following a velocity step decrease,
 771 for example, the gouge initially compacts, as for the quasi-normal grain size distribution, but then
 772 dilates by a greater amount to reach the new steady-state thickness. Where the signal-to-noise ratio
 773 is sufficient (e.g., Supplementary Figures S7-B and C, and to a lesser extent E and F), this transition
 774 from compaction to dilation seems to occur while the friction is monotonically (except for the noise)
 775 approaching its new steady state. The reverse behavior is seen for velocity step increases. We do
 776 not yet understand the origins of this behavior, and see no dramatic changes in the particle velocity
 777 profiles over the course of the non-monotonic thickness changes. The change in sign of $\delta d_n / \delta d_s$
 778 at these lower velocities, together with the monotonic nature of the (smoothed) friction (and hence
 779 state) transient, is inconsistent with the notion that state and porosity are linked in any simple way.
 780 Considering only the steady-state thickness changes (Figure 10B), the positive direct velocity effect
 781 (a stress increase for a velocity increase) is also inconsistent with the simple notion that the direct
 782 effect comes from sliding at the new velocity but the old porosity. However, this positive direct effect
 783 is consistent with the initial thickness change following a velocity step having the opposite sign than
 784 the steady-state thickness change (e.g., an initial thickness increase for a step velocity increase).

785 We ran one slide-hold simulation using the quasi-exponential grain size distribution, with ini-
 786 tial sliding velocity $V_i = 0.1$ m/s. It showed logarithmic-with-time stress relaxation and gouge
 787 compaction, with a compaction rate of about half that of the model with a quasi-normal grain size
 788 distribution, after normalizing by the different initial gouge thicknesses. Again considering only
 789 steady-state thickness changes in Figure 10B, this result seems inconsistent with the intuitive state-
 790 ment that the effect on gouge thickness of an order-of-magnitude increase in hold time is roughly
 791 comparable to the effect of an order-of-magnitude decrease in slip speed (Figure 2). And, as with
 792 the positive value of the direct velocity effect, the compaction during the hold seems qualitatively

793 consistent with the initial compaction following a step velocity decrease for the quasi-exponential
 794 grain size distribution; however, the subsequent dilation following the velocity step remains unex-
 795 plained.

796 5.3 Slide-hold simulations

797 The main emphasis of this paper has been granular simulations of velocity-step experiments,
 798 which have long been known to be well-modeled by the RSF framework using the Slip law for state
 799 evolution (A. Ruina, 1983; Bhattacharya et al., 2015). We have shown that the granular simulations,
 800 like the Slip law, predict that following the initial direct velocity response, friction decays quasi-
 801 exponentially to its new steady state over a slip distance that is independent of the magnitude and
 802 sign of the velocity step. Moreover, with apparently no important free parameters, the granular
 803 model with our adopted quasi-normal grain size distribution produces a direct velocity effect and a
 804 subsequent state evolution effect with amplitudes that vary linearly with the logarithm of the velocity
 805 jump, with values of the RSF parameters a and b that are reasonably close to those determined
 806 empirically in the laboratory. Changing to our quasi-exponential grain size distribution changes
 807 only the magnitudes of a and b , while still leaving them close to lab values (and perhaps introducing
 808 enough velocity dependence to make the system transition from steady-state velocity weakening to
 809 velocity strengthening with increasing slip speed).

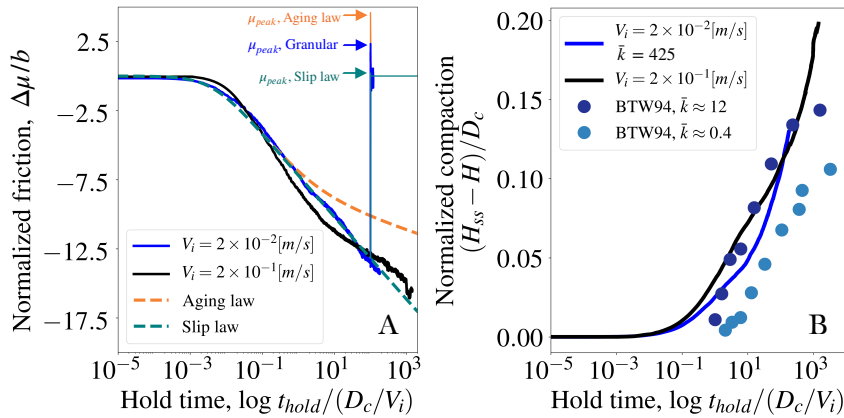


Figure 12. (A) The blue and black lines show the variation of friction coefficient, normalized by the RSF parameter b , as a function of normalized hold time, for granular slide-hold simulations with prior driving velocities V_i of 2×10^{-2} (blue) and 2×10^{-1} (black) m/s. The orange and green dashed lines show the predictions of the Slip and Aging laws, respectively, using the RSF parameters determined from the velocity step tests in Figure 4. This panel also shows (in blue) results of a reslide at $V = V_i = 2 \times 10^{-2}$ m/s following a normalized hold time $t_{hold}/(D_c/V_i)$ of 100, in comparison to the the Aging and Slip law predictions. The peak friction upon reslide is indicated by μ_{peak} . The confining pressure in all simulations is 5 MPa, and the dimensionless stiffness $\bar{k} \equiv k_{eff}D_c/(b\sigma) \approx 425$. (B) Blue and black lines show the change in gouge thickness during the slide-hold granular simulations of panel (A). (solid dots) The change in gouge thickness during hold experiments on granite reported by Beeler et al. (1994), who used two different (low and high) machine stiffnesses. An estimated slip-weakening distance $D_c \approx 3\mu\text{m}$ is used to normalize results from the laboratory experiments. Both low and high stiffness laboratory experiments were performed at 25 MPa confining pressure.

810 In this section, we present preliminary results from the default granular model using loading
 811 conditions intended to simulate slide-hold protocols. We focus on both the stress decay during the
 812 hold and the corresponding change in thickness of the gouge layer. Laboratory observations indi-
 813 cate that in response to an imposed load-point hold, the stress decays in a manner consistent with

814 the Slip law and not the Aging law, which exhibits too little decay due to time-dependent heal-
 815 ing (Bhattacharya et al., 2017). Furthermore, during the hold the gouge undergoes fault-normal
 816 compaction roughly as the logarithm of time. Although RSF classically makes no explicit pre-
 817 diction about fault-normal displacements, the conventional interpretation of log-time fault-normal
 818 compaction during holds is that it is consistent with the Aging law for state evolution. That is,
 819 compaction is viewed as going hand-in-hand with the plastic deformation of microscopic asperity
 820 contacts and log-time increase in true contact area under high local normal stresses (Berthoud et
 821 al., 1999; Sleep, 2006). This compaction is observed despite the fact that log-time healing as em-
 822 bodied by the Aging law for state evolution is ruled out by the stress data from the same slide-hold
 823 experiments.

824 We have thus far examined slide-hold simulations performed at two initial sliding velocities
 825 and $\sigma_n = 5$ MPa. Figure 12A shows the variation of normalized friction with normalized hold time
 826 for these tests, with the initial velocities of $V_i = 2 \times 10^{-2}$ m/s and 10^{-1} m/s shown by the blue and
 827 black curves, respectively. For standard RSF (equations 1–3 with constant parameter values), these
 828 curves would plot on top of one another when normalized in this fashion, a result that follows from
 829 dimensional analysis. Although the stress decay for the black curve ($V_i = 2 \times 10^{-1}$ m/s) is not strictly
 830 log-linear, a log-linear fit to that curve would be similar to the curve for $V_i = 2 \times 10^{-2}$ m/s. The figure
 831 also includes the predictions of the Aging and Slip laws, shown by the dashed orange and green
 832 lines, respectively, using the RSF parameter values determined independently from Slip law fits to
 833 the numerical velocity step tests. As described in the Computational Model section, for the RSF
 834 predictions we use a shear modulus of 300 MPa, leading to a normalized stiffness $\bar{k} = k_{\text{eff}} D_c / (b\sigma)$
 835 of 425. For a velocity-strengthening system with such a large stiffness, increasing (decreasing) \bar{k}
 836 by a factor of 2 shifts the Slip law fit left (right) by a slightly larger factor, but does not change the
 837 slope at long hold times (Bhattacharya et al., 2017, Appendix C2). The comparison between the
 838 blue and dashed green curves shows good agreement between the granular model and the Slip law
 839 prediction, as for the laboratory experiments of Beeler et al. (1994) analyzed by Bhattacharya et al.
 840 (2017). And the Aging law underestimates the stress decay during the holds, for the same reason
 841 that it underestimates the stress decay during lab experiments. This initial result suggests that the
 842 granular model, like the empirical Slip law, may capture much of the phenomenology of laboratory
 843 slide-hold tests. Further testing of the granular model over a broader range of slide/reslide velocities
 844 and spring stiffnesses, for comparison to available lab data, are currently underway.

845 In addition to seeming to match the stress decay during laboratory holds, the granular model
 846 qualitatively reproduces the observed reduction in gouge thickness with log hold time (Figure 12B).
 847 In the conventional RSF framework, because the stress data are well modeled by the Slip law with
 848 its lack of state evolution, the gouge would not be expected to compact. The paradox that it does so
 849 was also noted by Bhattacharya et al. (2017) in their analysis of the Beeler et al. (1994) slide-hold
 850 experiments. In contrast, and in agreement with laboratory experiments, our granular simulations
 851 show that log-time compaction during holds is present even though log-time healing as embodied by
 852 the Aging law is lacking. This behavior is reminiscent of the symmetric stress change/asymmetric
 853 thickness change in response to velocity step tests in Figure 4 (much more rapid variation in thick-
 854 ness than stress, following a step velocity decrease), and is another indication that equating state and
 855 porosity (Sleep, 2006; Lieou et al., 2017) neglects some fundamental aspect of granular friction.

856 5.3.1 Slide-hold-slide simulations

857 During both laboratory and simulated slide-hold-slide experiments, friction (shear stress) re-
 858 laxes during the hold, but upon the reslide overshoots its future steady-state value by an amount
 859 $\Delta\mu_{\text{peak}}$, reflecting the ‘healing’ (strengthening at a reference slip speed) of the gouge during the
 860 hold. As shown by Bhattacharya et al. (2017), neither the Aging law nor the Slip law can success-
 861 fully model, with a single set of parameter values, both the stress relaxation and the subsequent
 862 $\Delta\mu_{\text{peak}}$ for each of the high and low stiffness slide-hold-slide laboratory experiments of Beeler et
 863 al. (1994). In particular, although the Slip law can match the stress decay during holds for both
 864 stiffnesses moderately well, the predicted $\Delta\mu_{\text{peak}}$ for the high stiffness set-up is far too low to match

865 the lab data (figure 8a of Bhattacharya et al., 2017). The reason is that for the high-stiffness set-up,
 866 the slip during the load-point hold is too low for the Slip law to allow significant healing.

867 Figure 12A shows the predicted $\Delta\mu_{peak}$ for the granular simulation (blue), Aging law (orange)
 868 and Slip law (green), the latter two using the same values of a , b , and D_c used to model the holds.
 869 Note that the Slip law predicts $\Delta\mu_{peak} \sim 0$, because almost no slip accumulates during the load-point
 870 hold, and that $\Delta\mu_{peak}$ from the granular simulation is much higher. This is the first sliding protocol
 871 we have modeled for which the stress history from the granular simulation differs qualitatively from
 872 that of the Slip law, and it differs (1) in the sliding protocol for which the Slip law most obviously
 873 fails to match lab data (the reslides following holds); and (2) in the proper sense to match the lab
 874 data better than the Slip law.

875 5.4 Exploring the microphysics of granular rate-state friction

876 There is currently no well-accepted explanation for the empirical, but moderately successful,
 877 Slip law for describing the rate- and state-dependent frictional behavior of rock and gouge. The
 878 only heuristic explanation of which we are aware is that of Sleep (2006), who proposed that it
 879 results from the highly nonlinear stress-strain relation at contacting asperities (e.g., that the modestly
 880 smaller stress following a velocity step decrease results in an exponentially smaller strain rate, and
 881 a symmetric stress response to step increases and decreases when plotted against slip). In this paper
 882 we have presented a physical model that, despite lacking meaningful time-dependence at the contact
 883 scale, reproduces the Slip law where that law matches experimental data well (velocity-step and
 884 slide-hold protocols), and may outperform the Slip law where that law does not work (the reslides
 885 following holds). We would therefore like to use the output of the granular model to understand the
 886 source of its lab-like (and RSF-like) behavior.

887 As a first step, we consider the source of the rate-dependence of granular friction. We expect
 888 that the log-time densification and relaxation of stress during holds (and by extension the densifi-
 889 cation with decreasing slip speed during steady sliding) is due to a reduction of elastic potential
 890 energy associated with local grain rearrangements. These rearrangements generate seismic waves
 891 that perturb nearby grains which might themselves be near the threshold for hopping, at a rate
 892 that decays quasi-logarithmically with time, as the driving stress and the opportunities for contin-
 893 ued compaction lessen. This picture of grains as always vibrating, being perturbed by neighbors,
 894 and occasionally overcoming activation energy barriers, is conceptually similar to the traditional
 895 atomistic-scale view that the logarithmic rate-dependence in RSF (the $\log V/V_*$ term in Eq. 1) arises
 896 from a thermally-activated Arrhenius process (Rice et al., 2001; Lapusta et al., 2000; Chester, 1994).
 897 In that microscopic picture, the slip rate is $V = V_1 \exp(-E/(k_B T))$, where the product of the Boltz-
 898 mann constant, k_B , and the temperature, T , is a measure of the average kinetic energy (KE) of the
 899 atoms. The activation energy E has the form $E = E_1 - P\Omega_A$, where P is a representative pressure
 900 and Ω_A is the associated activation volume. In this equation, V_1 can be interpreted as an attempt
 901 frequency times a slip displacement per successful attempt. Such an interpretation reproduces the
 902 empirical logarithmic form of the direct velocity dependence of friction with

$$a = \frac{k_B T}{P\Omega_A}. \quad (17)$$

903 A histogram of the KE (E_k) of every grain in a steady-state granular simulation with $V_{lp} =$
 904 2×10^{-2} m/s is plotted on log-linear and log-log axes in Figs. 13A and B, respectively. Assuming
 905 that this KE plays the role of $k_B T$ in equation (17), we can use this measurement (mean value
 906 $\sim 2 \times 10^{-5}$ J/grain) to estimate a . We take the product of pressure and activation volume to be given
 907 by the elastic strain energy of grain compression, leading to

$$P\Omega_A \approx C \int_0^{\Delta_{ij}} F_n d(\delta_{ij}) = \frac{2}{5} CPd^3 \left[3(1 - \nu^2) \frac{P}{E} \right]^{2/3}, \quad (18)$$

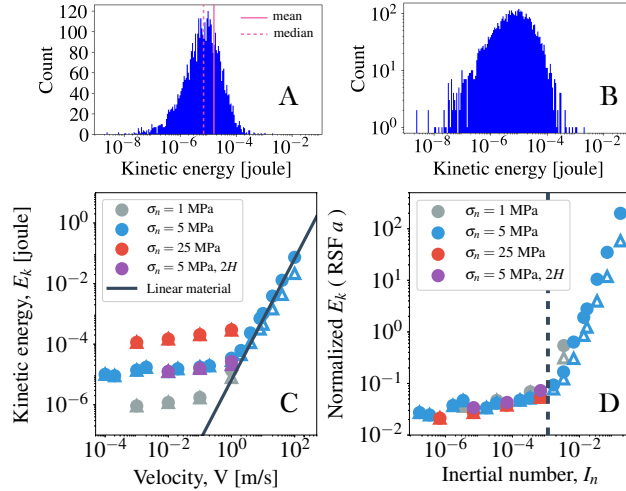


Figure 13. (A-B) Histograms of the per-grain KE during steady sliding at $V_{lp} = 2 \times 10^{-2}$ m/s in (A) log-linear (x-y) axes and (B) log-log axes. (C) The variation of the mean per grain KE (E_k) for steady-sliding simulations at a range of shearing velocities and confining pressures, as well as for a system with twice the size of the default model, compared to the estimate (solid line) of per grain KE assuming homogeneous shear between the driving plates. (D) The per grain KE, normalized by $P\Omega_A$ from equation 18 (our estimated RSF a), for the same steady-sliding simulations as in (C), here expressed as a function of the inertial number. The dashed line corresponds to $I_n = 10^{-3}$, which traditionally is considered the limit above which inertial effects become non-negligible. The upward-pointing triangles in (C) and (D) show the “fluctuating granular KE” (δE_k) as defined by Ogawa et al. (1980) and Ogawa (1978). In the low inertial number regime of interest, the difference between KE and δE_k is insignificant.

908 where C is the average coordination number (number of contacts per grain), Δ_{ij} is how closely
 909 two grain centers approach one another under the contact force F_n , $d()$ in the integral represents
 910 an infinitesimal change (not the grain diameter), and the last equality is derived using the nonlinear
 911 Hertzian contact law for F_n as a function of grain compression δ_{ij} (equation 8 with no damping,
 912 $d_i = d_j$, and $F_n = Pd^2$; d here is grain diameter). If we use D_{mean} for d , and $C \sim 4$ (a value
 913 obtained from our simulations), we find $a \sim 0.022$, close to the value determined independently
 914 from fitting our velocity-step tests.

915 There is certainly slop associated with this estimate, including whether the activation volume
 916 is more appropriately thought of as a single grain or a few grains that rearrange collectively (as in
 917 STZ theory), and whether it is the total normal displacement or the incremental displacement from
 918 the background state that determines the activation volume (similar questions pertain to the classical
 919 RSF estimate of a , e.g., whether the activation volume corresponds to a single atom or a unit cell).
 920 Nonetheless, we find the order-of-magnitude agreement to be encouraging. But this agreement is
 921 insufficient; if the granular KE is to play the role of temperature, it must be insensitive to both the
 922 sliding speed and the confining pressure, and it is not apparent that this need be the case. Empirically,
 923 however, we find that the mean value of granular KE at any particular P changes only modestly over
 924 several orders of magnitude variation in V_{lp} , at the low driving speeds of interest (Figure 13C). For
 925 comparison, the solid line on the same plot (of slope 2) shows the KE that would result from a layer
 926 of uniformly sheared grains as a function of V_{lp} . For $P = 5$ MPa the quasi-constant granular KE
 927 intersects this trend at $V_{lp} \sim 2$ m/s, the inertial number $I_n \sim 3 \times 10^{-3}$, and the system is traditionally
 928 considered to leave the regime of quasi-static flow (Forterre & Pouliquen, 2008). Furthermore, if
 929 we normalize the per grain KE by the estimate of $P\Omega_A$ from equation 18, as in (17), our proposed
 930 estimates of a collapse for all confining pressures onto a single curve in the quasi-static regime

(Figure 13D). The prediction is thus that a changes very slowly for a range of shearing velocities and pressures in the quasi-static regime, consistent with both our granular simulations and many laboratory rock and gouge friction experiments.

In Figure 13 we used mean grain kinetic energy as a measure of the effective temperature T_{eff} of the granular gouge. A number of more rigorous thermodynamics- and statistical mechanics-based relationships have been proposed for measuring T_{eff} in granular materials (e.g., the rate of change of energy with entropy); this remains an area of active research (Ono et al., 2002; Blumenfeld & Edwards, 2009; Puckett & Daniels, 2013; Bi et al., 2015). Ono et al. (2002) showed that for zero-temperature foam, seven of these definitions are internally consistent in that they yield the same variation of T_{eff} with shear rate. Further experimental investigations showed that two of these measures of T_{eff} become approximately constant at low shear rates (Song et al., 2005; Corwin et al., 2005). This is similar to our finding in Figure 13E, although these other measures are even more constant than our granular KE at low I_n . Such measurements are necessary to confirm whether different measures of temperature converge toward the same behavior, if they also agree with the variation of kinetic energy, and become nearly constant within the quasi-static regime. Such measurements could elaborate the cause of near constancy of the granular temperature – which to this date remains unknown – by making analogies to the behavior of other glassy materials (like foam) as they approach the glass transition.

6 Conclusions

In this work, we explored the frictional behavior of a granular gouge layer with no time-dependent plasticity at the grain-grain contact scale. We imposed velocity steps over a range of driving velocities and normal stresses that are relevant to earthquake nucleation and laboratory rock friction experiments. We further performed a limited number of slide-hold granular simulations. The system is mechanically stiff enough that, following a step change in driving velocity, the inelastic sliding velocity is essentially constant and variations in the friction coefficient are proportional to variations in log state. We found that the behavior of the granular model appears very similar to the Slip law version of the rate- and state-dependent friction equations, under conditions where the Slip law agrees well with laboratory data, *i.e.* velocity step and slide-hold tests. In particular, we observed that: (i) following velocity steps that vary by several orders of magnitude, friction approaches its future steady-state value over the same sliding distance (or strain, if gouge thickness is varied), (ii) the frictional response of the system to velocity-step increases and decreases is symmetric, (iii) the amplitude of frictional evolution following velocity steps scales with $\log(V_f/V_i)$, and (iv) the ranges of the RSF parameters a (0.020–0.029) and b (0.014–0.023) are not very different from those typically found in laboratory rock and gouge friction experiments. In addition, the slide-hold granular simulations appear to be well described by the Slip law, using parameters derived from fits to the velocity steps, as is the case (or nearly the case) for laboratory friction data. Finally, preliminary slide-hold-slide simulations indicate that the peak stress upon the reslide exceeds the prediction of the Slip law, using the same parameters that fit the hold well, as is also the case with lab data (Bhattacharya et al., 2017).

Future work should include investigating whether the granular model can reproduce observations of the friction peak upon the reslide in slide-hold-slide experiments (often referred to as ‘frictional healing’) (Marone & Saffer, 2015; Karner & Marone, 1998; Bhattacharya et al., 2017), over a broader range of normal stresses, driving velocities, and system stiffnesses than we have explored thus far; the recent observation that the slip-weakening distance following the reslide increases systematically with log hold time (Bhattacharya et al., 2017); and the friction and thickness changes observed in normal-stress stepping tests (B. Kilgore et al., 2017). These will be important tests for the granular model, as none of the current empirical constitutive relations for the behavior of rock interfaces reproduce these observations acceptably.

The conventional understanding that state evolution in RSF results from contact plasticity suggests that state and gouge thickness are closely related. However, we found that even though gouge thickness seems to be a useful proxy for variations in state following step velocity increases, the

982 gouge thickness evolves over much shorter slip distances than does friction following step decreases.
 983 Qualitatively, the asymmetric response of gouge thickness to velocity step increases and decreases
 984 appears similar to the asymmetric response of friction (i.e., log state) predicted by the Aging law.
 985 Related behavior is seen during load-point holds, where the friction coefficient appears to decay as
 986 predicted by the Slip law, implying very little state evolution, while the gouge layer compacts as log
 987 time, reminiscent of the (log) state increase predicted by the Aging law. The asymmetric response
 988 of the gouge thickness to changes in driving velocity, in conjunction with the symmetric response of
 989 the friction coefficient, indicates that gouge thickness is at best an incomplete description of state.
 990 The log-time compaction of the gouge during holds in which the friction decay is well described by
 991 a law that predicts very little state evolution suggests the same. Aspects of the granular structure
 992 other than porosity, such as force fabric and structural anisotropy, must also contribute to in the state
 993 of the system (Puckett & Daniels, 2013; Lechenault et al., 2006).

994 Both the asymmetric response of the gouge thickness to velocity step increases and decreases,
 995 and the log-time compaction during load point holds, are predictions of the granular model that seem
 996 consistent with laboratory rock and gouge friction experiments. Models of coupled fault gouge dila-
 997 tancy/pore pressure diffusion (e.g., Segall et al., 2010) are likely to be most consistent with existing
 998 lab experiments if porosity is tied to the Aging law for state evolution when state is increasing
 999 ($V\theta/D_c < 1$ in equations (2) and (3)), and the Slip law when state is decreasing ($V\theta/D_c > 1$), even
 1000 while the frictional strength is more accurately modeled by the Slip law under both conditions.

1001 We explored a range of parameters and material properties that could have influenced our ob-
 1002 servations. We found that grain-grain friction coefficient, restitution coefficient, and grain size had
 1003 only minor effects on system behavior. Using a system with roughly twice the thickness of the de-
 1004 fault model, we found that the critical slip distance scales with gouge thickness, and can instead be
 1005 expressed as a critical strain (of about 13%, when defined as D_c/H). We also examined the influ-
 1006 ence of changing the grain size distribution from a quasi-normal to a quasi-exponential distribution.
 1007 This reduced the value of a to about 0.008, near the low end of the range typically cited for rock
 1008 and gouge. More significantly, we found that changing from a quasi-normal to quasi-exponential
 1009 grain size distribution changed the steady-state friction from velocity-strengthening to something
 1010 closer to velocity-neutral. Although within the noise of the simulations the quasi-exponential sys-
 1011 tem could be argued to be strictly velocity-neutral, the close association between the observed
 1012 velocity-dependence of friction and the clearly non-monotonic steady-state gouge thickness leads
 1013 us to favor the interpretation that the steady state friction transitions from velocity-weakening to
 1014 velocity-strengthening with increasing slip speed. A non-monotonic dependence of steady-state
 1015 friction on driving velocity has not often been observed in numerical simulations of frictional gran-
 1016 ular systems (da Cruz et al., 2005; Kamrin & Koval, 2014; Koval et al., 2009; MiDi, 2004), but
 1017 within our adopted range of dimensionless pressures and inertial numbers it is consistent with re-
 1018 cent theoretical predictions (DeGiuli & Wyart, 2017). The effect of grain size distribution was not
 1019 explored by DeGiuli and Wyart (2017), however. In the velocity-strengthening regime, where the
 1020 quasi-exponential gouge layer dilates with increasing slip speed, following a velocity step the layer
 1021 approaches its new steady-state thickness monotonically, just as does the velocity-strengthening
 1022 gouge with the quasi-normal size distribution. In the velocity-weakening regime, however, the
 1023 gouge thickness for the quasi-exponential system varies non-monotonically following a velocity
 1024 step, for example first compacting following a step decrease before dilating by a larger amount with
 1025 continued slip. This initial response seems consistent with a positive direct velocity effect, and is
 1026 consistent with the observed compaction during holds for the quasi-exponential system, but the non-
 1027 monotonic evolution of thickness with slip is yet another indication that there is not a simple relation
 1028 between gouge porosity and state, and we do not understand its cause.

1029 By making an analogy between granular rearrangements in a potential energy landscape and a
 1030 thermally-activated Arrhenius process, we estimated the magnitude of direct velocity effect (the RSF
 1031 parameter a) in our model. For this purpose, we used the mean kinetic energy of grains as a measure
 1032 of granular temperature, and assumed that this was equivalent to the thermodynamic temperature
 1033 in a thermally-activated process. We found a value of a close to that obtained independently from
 1034 fitting our velocity-step tests. Furthermore, this value was found to be independent of confining

1035 stress and nearly independent of slip speed. This nearly constant value of a is consistent with our
1036 simulation results and with much lab data.

1037 The successful adoption here of the granular temperature may motivate its future implementa-
1038 tion as a state variable for granular rate- and state-dependent friction. In standard thermodynamics,
1039 involving thermal materials, energy is the conserved property. However, the granular materials in
1040 our simulations, and in many others in the physics literature, are athermal, in the sense that the ac-
1041 tual temperature plays no role. Recent progress in the granular physics community points toward a
1042 revised version of granular temperature, called *keramicity* and defined in the stress ensemble, where
1043 instead of energy the conserved quantity is the force-moment tensor of the granular packing (Bi
1044 et al., 2015). Ideally, one would like to devise a state variable that would obey the laws of ther-
1045 modynamics for granular systems and be path- and protocol-independent. It would be interesting
1046 to investigate whether a state variable defined in the stress ensemble could be used for effectively
1047 describing the rate- and state-dependent frictional behavior of rocks.

1048 While our observations here focused on rock gouge and the frictional behavior of fault rocks,
1049 they could be potentially relevant for transient frictional behavior and hysteresis of a broad range
1050 of disordered Earth materials, such as soils on hillslopes (Ferdowsi et al., 2018; Handwerker et al.,
1051 2016), fluvial sediments (Houssais et al., 2015; J. P. Johnson, 2016; Masteller et al., 2019), and
1052 sub-glacial till (Rathbun et al., 2008).

1053 Appendix A Dimensionless parameters

1054 The adopted DEM model has many dimensionless parameters, each of which could potentially
1055 affect the system behavior. However, only a few of these seem to be significant. Here we give a
1056 full accounting of these parameters, along with a qualitative assessment of their relevance to the
1057 observed RSF parameters in the slow shearing regime of interest.
1058

1059 Table A1. DEM parameters for steady-sliding simulations.

Symbol	Parameter	Units
D	Median grain diameter	[m]
H	Nominal gouge thickness	[m]
L_x	Domain length in slip direction	[m]
L_y	Domain length in slip-perpendicular direction	[m]
k_n	Grain normal contact stiffness	[Pa]
k_t	Grain shear contact stiffness	[Pa]
ϵ_n	Grain normal restitution coefficient	[]
ϵ_t	Grain shear restitution coefficient	[]
μ_g	Grain-grain friction coefficient	[]
ρ	Grain density	[kg m ⁻³]
V_{lp}	Driving velocity	[m s ⁻¹]
$\sigma_n (P)$	Applied normal stress	[Pa]
k_{sp}	Driving spring stiffness	[Pa m ⁻¹]
g	Gravitational acceleration	[m s ⁻²]
Δt	Numerical time step	[s]

1061 Neglecting parameters associated with the adopted grain size distribution, Table A1 lists 15 in-
1062 dependent dimensional parameters using 3 dimensions (writing Pa as kg m⁻¹ s⁻²), implying that 12
1063 dimensionless parameters govern the system. Some of the parameters in Table A1 can be considered
1064 as equivalent to an equal number of different parameters; for example, the grain normal and shear
1065 contact stiffnesses are derived from the elastic shear and Young's moduli (G and E), and the normal
1066 and shear restitution coefficients are derived from the normal and shear damping coefficients γ_n and

1067 γ_t . Additional parameters depend upon those listed; for example, the grain mass m and the bulk
 1068 density ρ_H and shear modulus G_H , as well as the measured friction coefficient.

1069 Before listing dimensionless parameters, we introduce some relevant time scales:

- 1070 1. t_γ , time scale for bulk strain of 1: H/V_{lp} .
- 1071 2. t_w , time scale for elastic shear wave propagation across layer: $H/\sqrt{G_H/\rho_H}$.
- 1072 3. t_i , inertial time scale for an initially stationary a grain to move a distance D , given an applied
 1073 force PD^2 : $D\sqrt{\rho/P}$
- 1074 4. t_{col} , collision time (obtained by solving equation (12) in the text).

1075 Table A2 lists a reasonable set of choices for the 12 dimensionless parameters. Three involve
 1076 ratios of lengths. It has been proposed that the ratio H/D determines the ability of the gouge to
 1077 localize deformation, with no localization for values $\lesssim 10$ (Tsai & Gollub, 2005). We see no lo-
 1078 calization in the velocity profiles for our default model with $H/D \sim 13.3$, or in the model with
 1079 $H/D = 24$ and L_x/H and L_y/H unchanged. We also see no change in the RSF parameters between
 1080 the two simulations, provided we speak of a critical strain rather than a critical slip distance D_c (Fig-
 1081 ure 6). The ratios L_x/H and L_y/H are not expected to be significant as long as they are sufficiently
 1082 large; if force chains typically form at $\sim 45^\circ$ then L_x/H should at a minimum exceed 1. We see no
 1083 significant difference between $L_x/H = 1.5$ and $L_x/H = 5$ for both normal and exponential grain size
 1084 distributions, other than the expected result that simulations with $L_x/H = 5$ exhibit less variability
 1085 during steady sliding.
 1086

1087 Table A2. DEM governing parameters.

H/D ; L_x/H ; L_y/H
ϵ_n ; ϵ_t ; μ_g
k_n/k_t ; $k_{sp}/(G/H)$; $\rho gH/P$
$\Delta t/t_c$
t_i/t_γ (Inertial number I_n , equal to $(V_{lp}/H)D\sqrt{\rho/P}$)
$(P/E)^{2/3}$ (dimensionless pressure)

1089 We have varied ϵ_n over nearly the full range of 0 to 1. Consistent with previous results for
 1090 steady-state friction (MiDi, 2004), we find negligible influence of the restitution coefficients on
 1091 the RSF parameters in the low- I_n regime of interest (Supplementary Figure S3). We have always
 1092 assumed that the damping coefficients satisfy $\gamma_t = 0.5\gamma_n$, the default for LAMMPS, from which the
 1093 restitution coefficients are derived, but given the existing results we expect no significant change for
 1094 $\gamma_t \neq 0.5\gamma_n$. We also see no significant changes in the RSF parameters when doubling μ_g from the
 1095 default value of 0.5 to 1.0 (Supplementary Figure S6). This is consistent with previous studies that
 1096 show little influence of μ_g on steady-state friction (MiDi, 2004).

1097 The ratio k_n/k_t is fixed by the elastic moduli of the grains and is not a free parameter. The
 1098 ratio $k_{sp}/(G/H)$ controls the elastic deformation of the driving spring to that of the gouge layer
 1099 (the more relevant bulk gouge shear modulus G_H depends upon G and the granular packing). We
 1100 made k_{sp} extremely large, to make the effective stiffness of the system as large as possible; this
 1101 ensures that sliding velocity following a step change in V_{lp} is constant, such that changes in friction
 1102 correspond directly to changes in $\log(\text{state})$, facilitating a “by eye” comparison of the measured
 1103 friction transient to different state evolution laws. Significantly reducing $k_{sp}/(G/H)$ will change the
 1104 loading history of the gouge layer for a given V_{lp} history, but traditionally the RSF parameters are
 1105 assumed to be independent of loading history. The ratio $\rho gH/P$ determines the relative magnitude
 1106 of the gravitational stress at the base of the gouge layer to the applied stress; in our simulations it is
 1107 so low (10^{-6} to 10^{-8}) that we expect it to be negligible, although it may lead to some grain sorting

1108 during the packing of the gouge layer prior to imposing the confining pressure. In the future it would
1109 make sense to dispense with gravity during the sliding and most of the packing phases.

1110 For numerical accuracy we employ $\Delta t/t_{col} = 0.01$, small enough that it does not influence the
1111 simulations.

1112 The inertial number I_n , equal to t_i/t_γ , is a well-established control parameter for granular
1113 systems, but from the figures in this paper it does not affect the RSF parameters much. This is
1114 consistent with many laboratory rock and gouge friction experiments.

1115 The dimensionless pressure $(P/E)^{2/3}$ is equal to the grain strain (grain compression at a contact
1116 divided by the initial grain radius) under the Hertzian contact law. For P from 1 to 50 MPa, this ratio
1117 varies from 0.7×10^{-3} to 10^{-2} , near to but perhaps not within the “rigid grain” limit (DeGiuli &
1118 Wyart, 2017). We find that the RSF parameters vary only modestly, and not necessarily consistently,
1119 over this interval (Table 5.2.1).

1120 This information can be used to extrapolate beyond the simulations already run. For example,
1121 we use a relatively large D_{mean} of 3 mm, but from Table A2, if we reduce the grain size and all model
1122 dimensions by the same factor (say 2 orders of magnitude) and keep V_{pl} and all other parameters
1123 the same, we change nothing other than to increase $k_{sp}/(G_H/H)$ and decrease $\rho g H/P$ by the same
1124 2 orders of magnitude. These ratios were already so large and so small that we expect to see no
1125 significant changes to the model output, consistent with Figure 9.

1126 In summary, despite the large number of dimensionless parameters in Table A2, remarkably few
1127 of these are free parameters available for tuning the values of the RSF coefficients. Their influence
1128 might be largest on the value of $(a-b)$, as this depends upon the difference between two numbers of
1129 comparable magnitude. Significantly, the sign of $(a-b)$ seems sensitive to the grain size distribution.
1130 This is a parameter that, along with grain shape and perhaps others, is not referenced in Table A1.

1131 Appendix B The inertial contribution to the measured shear stress

1132 Equation (13) in the main text assumes that the elastic component of the gouge deformation
1133 occurs quasi-statically and uniformly across the gouge, such that for constant load-point and sliding
1134 velocities the shear stress increases linearly with time and load-point displacement. However, for
1135 a linearly elastic system, following a sudden change of upper plate velocity ΔV_{pl} , a shear wave
1136 traverses the layer that, until the arrival of the reflected wave from the stationary lower plate, imposes
1137 an instantaneous shear stress change at the base of the upper plate given by

$$\Delta \tau_{inertial} = G_H \frac{\Delta V_{pl}}{\beta} = \Delta V_{pl} \sqrt{G_H \rho_H}, \quad (B1)$$

1138 where $\beta = \sqrt{G_H/\rho_H}$ is the elastic shear wave speed, with G_H being the shear modulus and ρ_H the
1139 density of the gouge layer (Rice, 1993). Dividing this by the normal stress gives an estimate of the
1140 inertial contribution to the “apparent” direct velocity effect,

$$\Delta \mu_{inertial} = \Delta V_{pl} \sqrt{G_H \rho_H} / \sigma_n. \quad (B2)$$

1141 For the example of the 4-order velocity increase to $V_f = 2$ m/s in Figure 3A, we see an instantaneous,
1142 not linear-with-time, apparent $\Delta \mu_{inertial}$ of about 0.19. Plugging this value into the left side of (B2),
1143 and on the right 5 MPa for σ_n and a typical porosity of 0.45 to estimate ρ_H , we calculate $G_H = 165$
1144 MPa. This is just over half the 270-310 MPa we estimated from the reloading (at much lower slip
1145 speeds) of the gouge following long holds (Figure B1), but it is certainly possible that at the large
1146 stresses associated with the 4-order velocity jump, some inelastic deformation is occurring.

1147 Note that Figure 9B shows a snapshot in which the shear wave front following a 1-order ve-
1148 locity jump (to 0.1 m/s) has yet to traverse the gouge layer. The post-jump displacement of the

1149 upper plate is $10^{-3}D_{mean}$, or 3×10^{-6} m, in (at $V_{Ip} = 0.1$ m/s) 3×10^{-5} s, and the shear wave has
 1150 progressed approximately 0.02 m, implying a propagation velocity of ~ 670 m/s. Setting this equal
 1151 to $\sqrt{G_H/\rho_H}$ and estimating ρ_H as above, we can derive a third independent estimate of G_H : 610
 1152 MPa, about twice the estimate from Figure B1. As we have not investigated in detail the nature of
 1153 the shear wave propagation across the gouge layer, we continue to use our mid-range estimate of
 1154 $G_H \sim 300$ MPa, consistent with our nearly quasi-static reloading simulations ($V_{Ip} = 2 \times 10^{-2}$ m/s),
 1155 with previous experimental, numerical, and theoretical estimates for granular systems under compar-
 1156 able conditions (Yin, 1993; Domenico, 1977; Makse et al., 1999), and with standard methods
 1157 of estimating G in laboratory rock and gouge friction experiments (e.g., Bhattacharya et al., 2017).
 1158 As we note in the main text, 300 MPa is large enough that variations in G_H of a factor of 2 do not
 1159 change the Slip law fits to our simulated velocity steps, and do not change the slope of the slip law
 1160 prediction at large hold times in Figure 12.

1161 It is clear that for any value of G_H in the vicinity of 300 MPa, for $V_f = 2$ m/s inertia contributes
 1162 significantly to the apparent $\Delta\mu$ for early times. However, note that once the steady-state velocity
 1163 profile in the gouge is reached, the contribution from bulk inertia to the measured $\Delta\mu$ at later times
 1164 is zero. The approach to that steady-state velocity profile is likely a complex process involving
 1165 multiple reflections from the bounding rigid plates. We can make an estimate of $\Delta\mu_{inertial}$ in this
 1166 case from the inertial force per area A required to change the velocity profile from one steady state
 1167 to another over a time Δt :

$$\Delta\mu_{inertial} = \frac{m\ddot{x}}{\sigma_n A} = \frac{\rho_H H}{\sigma_n} \frac{\Delta V_{pl}/2}{\Delta t}, \quad (\text{B3})$$

1168 where \ddot{x} is the spatially-averaged acceleration of the gouge particles and $\Delta V_{pl}/2$ comes from as-
 1169 suming the steady-state velocity profile to vary linearly across the gouge layer. Note that $\Delta\mu_{inertial}$
 1170 is proportional to $1/\Delta t$ as well as to ΔV_{pl} . For example, peak friction for $V_f = 2$ m/s in Figure 3
 1171 is reached at 6×10^{-4} s. If this is the time at which the steady-state velocity profile is reached (roughly
 1172 5 times the 2-way shear wave travel time across the gouge as estimated from Figure 9B), the inertial
 1173 contribution to the apparent $\Delta\mu$ would average only 0.018 up to that point (11% of the plotted peak
 1174 value), would likely be lower at that slip distance, and would be zero at greater distances. If the
 1175 steady-state velocity profile was not reached until a slip distance of D_{mean} , the contribution to the
 1176 measured friction up to that point would average more than a factor of two smaller. In light of these
 1177 results, we conclude that inertia can contribute modestly (or zero) to the measured friction in the
 1178 vicinity of the friction peak for $V_f = 2$ m/s in Figure 3, but that it provides a negligible contribution
 1179 to the overall Slip law fit to that friction curve.

1180 For the 10-times-smaller jump to $V_f = 0.2$ m/s, the inertial contribution to the measured friction
 1181 would be 10 times smaller from equation (B2), as well as from (B3) assuming that the same time
 1182 Δt is required to reach the new steady-state velocity profile. For this velocity step the peak friction
 1183 does not occur until a slip distance of $\sim 0.4D_{mean}$, at which point the steady-state velocity profile
 1184 is almost certainly established (see Figures 9C and D for velocity profiles at slip distances 40 and 4
 1185 times smaller, for $V_f = 0.1$ m/s), and the contribution from bulk inertia would be zero (if not, from
 1186 (B3) the average contribution up to that point would be 0.0019, which at the scale of Figure 3A
 1187 is completely negligible). We conclude that bulk inertia plays no discernible role in our simulated
 1188 velocity steps where the larger (initial or final) slip speed is 0.2 m/s or smaller, and that even at 2 m/s
 1189 inertia will only affect the friction curves significantly for slip distances smaller than some tenths of
 1190 D_{mean} .

1191 Acknowledgments

1192 BF acknowledges support from the Department of Geosciences, Princeton University, in form of a
 1193 Harry H. Hess postdoctoral fellowship, and from NSF award EAR-1547286 and the US Geological
 1194 Survey (USGS), Department of the Interior, award G19AP00048, both to AMR. BF performed
 1195 some slide-hold-slide tests during his PhD research with the granular physics model he developed
 1196 in his PhD. Some elements of the current model, which is distinct from the model in his PhD,

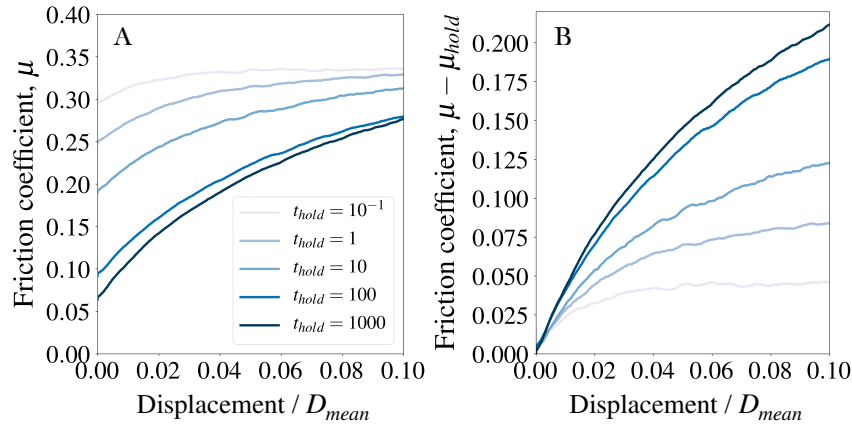


Figure B1. (A) The variation of friction coefficient with load-point displacement for the reslide portion of several slide-hold-reslide simulations (obtained from the default model with $V_{lp} = 2 \times 10^{-2}$ m/s and $\sigma_n = 5$ MPa). In (B), the friction coefficient at the end of the hold is subtracted from the signals, so the initial slopes of the reslide curves can be more easily compared. From the asymptotic slope at zero displacement (using the longest hold over a load-point displacement of $0.008D_{mean}$) we estimate an elastic shear modulus of $\sim 270 - 310$ MPa.

1197 were developed during BF's stay at the University of Pennsylvania, partially supported by the 2016
 1198 Southern California Earthquake Center (SCEC) award 16059 to David L. Goldsby. A study on
 1199 the granular origins of rate- and state-dependent friction for fault gouge was also proposed in that
 1200 same award to David L. Goldsby. BF benefited from conversations with Chris Marone, Pathikrit
 1201 Bhattacharya, Anders Damsgaard, Nicholas M. Beeler, Heather Savage, Emily Brodsky, Andrea J.
 1202 Liu, Corey O'Hern, Troy Shinbrot, Norman Sleep, Rob Skarbek, Paul Segall, Karen E. Daniels,
 1203 Shmuel Rubinstein, Rob Viesca, Melodie French, Julia Morgan, Jean M. Carlson, Ahmed Elbanna,
 1204 Andreas Kronenberg, David Sparks, and Hiroko Kitajima. AR benefited from a subset of those. BF
 1205 would also like to acknowledge support he has received from D. J. Jerolmack and D. L. Goldsby,
 1206 and the insightful discussions he had with D. J. Jerolmack, D. L. Goldsby, C. A. Thom, and Carlos
 1207 P. Ortiz on this topic during 2015-2016. Parallel programs were run on computers provided by the
 1208 Princeton Institute for Computational Science and Engineering (PICSciE). The 3-D visualizations of
 1209 the model were performed using the open-source visualization software "The Persistence of Vision
 1210 Raytracer" POV-Ray (<http://www.povray.org>). Most of the data analysis were carried out using
 1211 the open-source Python library, NumPy (<https://numpy.org>). The 2-D plots were made with the
 1212 Python library Matplotlib (www.matplotlib.org). The computer codes for LAMMPS simulations
 1213 of this paper with the information about the version of LAMMPS used for the simulations, are
 1214 available on the Dryad digital repository at <https://doi.org/10.5061/dryad.2z34tmphk>. We thank two
 1215 anonymous reviewers whose suggestions helped to improve and clarify this paper. The views and
 1216 conclusions contained in this document are those of the authors and should not be interpreted as
 1217 necessarily representing the official policies, either expressed or implied, of the U.S. Government.

1218 References

- 1219 Abe, S., Dieterich, J. H., Mora, P., & Place, D. (2002). Simulation of the influence of rate-and
 1220 state-dependent friction on the macroscopic behavior of complex fault zones with the lattice
 1221 solid model. *pure and applied geophysics*, 159(9), 1967–1983.
- 1222 Abe, S., & Mair, K. (2009). Effects of gouge fragment shape on fault friction: New 3d modelling
 1223 results. *Geophysical Research Letters*, 36(23).
- 1224 Aghababaei, R., Brink, T., & Molinari, J.-F. (2018). Asperity-level origins of transition from mild
 1225 to severe wear. *Physical review letters*, 120(18), 186105.

- 1226 Aharonov, E., & Sparks, D. (2002). Shear profiles and localization in simulations of granular
1227 materials. *Physical Review E*, 65(5), 051302.
- 1228 Aharonov, E., & Sparks, D. (2004). Stick-slip motion in simulated granular layers. *Journal of*
1229 *Geophysical Research: Solid Earth*, 109(B9).
- 1230 Amon, A., Bruand, A., Crassous, J., Clément, E., et al. (2012). Hot spots in an athermal system.
1231 *Physical review letters*, 108(13), 135502.
- 1232 Ampuero, J.-P., & Rubin, A. M. (2008). Earthquake nucleation on rate and state faults—aging and
1233 slip laws. *Journal of Geophysical Research: Solid Earth*, 113(B1).
- 1234 An, L.-J., & Sammis, C. G. (1994). Particle size distribution of cataclastic fault materials from
1235 southern california: A 3-d study. *Pure and Applied Geophysics*, 143(1-3), 203–227.
- 1236 Anthony, J. L., & Marone, C. (2005). Influence of particle characteristics on granular friction.
1237 *Journal of Geophysical Research: Solid Earth*, 110(B8).
- 1238 Baumberger, T., Berthoud, P., & Caroli, C. (1999). Physical analysis of the state-and rate-dependent
1239 friction law. ii. dynamic friction. *Physical Review B*, 60(6), 3928.
- 1240 Baumberger, T., & Caroli, C. (2006). Solid friction from stick–slip down to pinning and aging.
1241 *Advances in Physics*, 55(3-4), 279–348.
- 1242 Beeler, N., & Tullis, T. (1997). The roles of time and displacement in velocity-dependent volumetric
1243 strain of fault zones. *Journal of Geophysical Research: Solid Earth*, 102(B10), 22595–22609.
- 1244 Beeler, N., Tullis, T., Blanpied, M., & Weeks, J. (1996). Frictional behavior of large displacement
1245 experimental faults. *Journal of Geophysical Research: Solid Earth*, 101(B4), 8697–8715.
- 1246 Beeler, N., Tullis, T., & Weeks, J. (1994). The roles of time and displacement in the evolution effect
1247 in rock friction. *Geophysical Research Letters*, 21(18), 1987–1990.
- 1248 Behringer, R. P., Bi, D., Chakraborty, B., Henkes, S., & Hartley, R. R. (2008). Why do granular
1249 materials stiffen with shear rate? test of novel stress-based statistics. *Physical review letters*,
1250 101(26), 268301.
- 1251 Berthoud, P., Baumberger, T., G'sell, C., & Hiver, J.-M. (1999). Physical analysis of the state-and
1252 rate-dependent friction law: Static friction. *Physical review B*, 59(22), 14313.
- 1253 Bhattacharya, P., Rubin, A. M., Bayart, E., Savage, H. M., & Marone, C. (2015). Critical evaluation
1254 of state evolution laws in rate and state friction: Fitting large velocity steps in simulated
1255 fault gouge with time-, slip-, and stress-dependent constitutive laws. *Journal of Geophysical*
1256 *Research: Solid Earth*, 120(9), 6365–6385.
- 1257 Bhattacharya, P., Rubin, A. M., & Beeler, N. M. (2017). Does fault strengthening in laboratory rock
1258 friction experiments really depend primarily upon time and not slip? *Journal of Geophysical*
1259 *Research: Solid Earth*.
- 1260 Bi, D., Henkes, S., Daniels, K. E., & Chakraborty, B. (2015). The statistical physics of athermal
1261 materials. *Annu. Rev. Condens. Matter Phys.*, 6(1), 63–83.
- 1262 Bililign, E. S., Kollmer, J. E., & Daniels, K. E. (2019). Protocol dependence and state variables in
1263 the force-moment ensemble. *Physical review letters*, 122(3), 038001.
- 1264 Billi, A. (2005). Grain size distribution and thickness of breccia and gouge zones from thin (≈ 1 m)
1265 strike-slip fault cores in limestone. *Journal of Structural Geology*, 27(10), 1823–1837.
- 1266 Blanpied, M., Marone, C., Lockner, D., Byerlee, J., & King, D. (1998). Quantitative measure of the
1267 variation in fault rheology due to fluid-rock interactions. *Journal of Geophysical Research:*
1268 *Solid Earth*, 103(B5), 9691–9712.
- 1269 Blumenfeld, R., & Edwards, S. F. (2009). On granular stress statistics: Compactness, angoricity,
1270 and some open issues. *The Journal of Physical Chemistry B*, 113(12), 3981–3987.
- 1271 Bouzid, M., Izzet, A., Trulsson, M., Clément, E., Claudin, P., & Andreotti, B. (2015). Non-local
1272 rheology in dense granular flows. *The European Physical Journal E*, 38(11), 125.
- 1273 Brilliantov, N. V., Spahn, F., Hertzsch, J.-M., & Pöschel, T. (1996). Model for collisions in granular
1274 gases. *Physical review E*, 53(5), 5382.
- 1275 Chester, F. M. (1994). Effects of temperature on friction: Constitutive equations and experiments
1276 with quartz gouge. *Journal of Geophysical Research: Solid Earth*, 99(B4), 7247–7261.
- 1277 Corwin, E. I., Jaeger, H. M., & Nagel, S. R. (2005). Structural signature of jamming in granular
1278 media. *Nature*, 435(7045), 1075.
- 1279 da Cruz, F., Emam, S., Prochnow, M., Roux, J.-N., & Chevoir, F. (2005). Rheophysics of dense gran-
1280 ular materials: Discrete simulation of plane shear flows. *Physical Review E*, 72(2), 021309.

- 1281 Darnige, T., Bruand, A., Clement, E., et al. (2011). Creep and fluidity of a real granular packing
1282 near jamming. *Physical review letters*, *107*(13), 138303.
- 1283 Daub, E. G., & Carlson, J. M. (2008). A constitutive model for fault gouge deformation in dynamic
1284 rupture simulations. *Journal of Geophysical Research: Solid Earth*, *113*(B12).
- 1285 de Coulomb, A. F., Bouzid, M., Claudin, P., Clément, E., & Andreotti, B. (2017). Rheology of
1286 granular flows across the transition from soft to rigid particles. *Physical Review Fluids*, *2*(10),
1287 102301.
- 1288 DeGiuli, E., & Wyart, M. (2017). Friction law and hysteresis in granular materials. *Proceedings of
1289 the National Academy of Sciences*, *114*(35), 9284–9289.
- 1290 Dieterich, J. (1994). A constitutive law for rate of earthquake production and its application to
1291 earthquake clustering. *Journal of Geophysical Research: Solid Earth*, *99*(B2), 2601–2618.
- 1292 Dieterich, J. H. (1972). Time-dependent friction in rocks. *Journal of Geophysical Research*, *77*(20),
1293 3690–3697.
- 1294 Dieterich, J. H. (1978). Time-dependent friction and the mechanics of stick-slip. In *Rock friction
1295 and earthquake prediction* (pp. 790–806). Springer.
- 1296 Dieterich, J. H. (1979). Modeling of rock friction: 1. experimental results and constitutive equations.
1297 *Journal of Geophysical Research: Solid Earth*, *84*(B5), 2161–2168.
- 1298 Dieterich, J. H. (1992). Earthquake nucleation on faults with rate-and state-dependent strength.
1299 *Tectonophysics*, *211*(1-4), 115–134.
- 1300 Dieterich, J. H., & Kilgore, B. (1996). Implications of fault constitutive properties for earthquake
1301 prediction. *Proceedings of the National Academy of Sciences*, *93*(9), 3787–3794.
- 1302 Dieterich, J. H., & Kilgore, B. D. (1994). Direct observation of frictional contacts: New insights for
1303 state-dependent properties. *Pure and Applied Geophysics*, *143*(1-3), 283–302.
- 1304 Dieterich, J. H., et al. (1981). Constitutive properties of faults with simulated gouge. *Mechanical
1305 Behavior of*.
- 1306 Dijkstra, J. A., Wortel, G. H., van Dellen, L. T., Dauchot, O., & van Hecke, M. (2011). Jamming,
1307 yielding, and rheology of weakly vibrated granular media. *Physical review letters*, *107*(10),
1308 108303.
- 1309 Domenico, S. (1977). Elastic properties of unconsolidated porous sand reservoirs. *Geophysics*,
1310 *42*(7), 1339–1368.
- 1311 Ferdowsi, B., Griffa, M., Guyer, R., Johnson, P., Marone, C., & Carmeliet, J. (2013). Microslips as
1312 precursors of large slip events in the stick-slip dynamics of sheared granular layers: A discrete
1313 element model analysis. *Geophysical Research Letters*, *40*(16), 4194–4198.
- 1314 Ferdowsi, B., Ortiz, C. P., & Jerolmack, D. J. (2018). Glassy dynamics of landscape evolution.
1315 *Proceedings of the National Academy of Sciences*, *115*(19), 4827–4832.
- 1316 Forterre, Y., & Pouliquen, O. (2008). Flows of dense granular media. *Annu. Rev. Fluid Mech.*, *40*,
1317 1–24.
- 1318 Frye, K. M., & Marone, C. (2002). Effect of humidity on granular friction at room temperature.
1319 *Journal of Geophysical Research: Solid Earth*, *107*(B11), ETG–11.
- 1320 Handwerker, A. L., Rempel, A. W., Skarbak, R. M., Roering, J. J., & Hilley, G. E. (2016). Rate-
1321 weakening friction characterizes both slow sliding and catastrophic failure of landslides. *Pro-
1322 ceedings of the National Academy of Sciences*, *113*(37), 10281–10286.
- 1323 Hartley, R., & Behringer, R. (2003). Logarithmic rate dependence of force networks in sheared
1324 granular materials. *Nature*, *421*(6926), 928.
- 1325 Hatano, T. (2007). Power-law friction in closely packed granular materials. *Physical Review E*,
1326 *75*(6), 060301.
- 1327 Hatano, T. (2009). Scaling of the critical slip distance in granular layers. *Geophysical Research
1328 Letters*, *36*(18).
- 1329 Hatano, T. (2015). Friction laws from dimensional-analysis point of view. *Geophysical Journal
1330 International*, *202*(3), 2159–2162.
- 1331 Hazzard, J. F., & Mair, K. (2003). The importance of the third dimension in granular shear. *Geo-
1332 physical Research Letters*, *30*(13).
- 1333 Heslot, F., Baumberger, T., Perrin, B., Caroli, B., & Caroli, C. (1994). Creep, stick-slip, and dry-
1334 friction dynamics: Experiments and a heuristic model. *Physical review E*, *49*(6), 4973.

- 1335 Houssais, M., Ortiz, C. P., Durian, D. J., & Jerolmack, D. J. (2015). Onset of sediment transport is
 1336 a continuous transition driven by fluid shear and granular creep. *Nature communications*, *6*.
- 1337 Johnson, J. P. (2016). Gravel threshold of motion: a state function of sediment transport disequilibrium?
 1338 *Earth Surface Dynamics*, *4*(3), 685–703.
- 1339 Johnson, K. L. (1987). *Contact mechanics*. Cambridge University Press.
- 1340 Kamrin, K., & Koval, G. (2014). Effect of particle surface friction on nonlocal constitutive behavior
 1341 of flowing granular media. *Computational Particle Mechanics*, *1*(2), 169–176.
- 1342 Karner, S. L., & Marone, C. (1998). The effect of shear load on frictional healing in simulated fault
 1343 gouge. *Geophysical research letters*, *25*(24), 4561–4564.
- 1344 Kato, N., & Tullis, T. E. (2001). A composite rate-and state-dependent law for rock friction.
 1345 *Geophysical research letters*, *28*(6), 1103–1106.
- 1346 Kilgore, B., Beeler, N. M., Lozos, J., & Oglesby, D. (2017). Rock friction under variable normal
 1347 stress. *Journal of Geophysical Research: Solid Earth*, *122*(9), 7042–7075.
- 1348 Kilgore, B. D., Blanpied, M. L., & Dieterich, J. H. (1993). Velocity dependent friction of granite
 1349 over a wide range of conditions. *Geophysical Research Letters*, *20*(10), 903–906.
- 1350 Koval, G., Roux, J.-N., Corfdir, A., & Chevoir, F. (2009). Annular shear of cohesionless granular
 1351 materials: From the inertial to quasistatic regime. *Physical Review E*, *79*(2), 021306.
- 1352 Kuwano, O., Ando, R., & Hatano, T. (2013). Crossover from negative to positive shear rate dependence
 1353 in granular friction. *Geophysical research letters*, *40*(7), 1295–1299.
- 1354 Landau, L. D., & Lifshitz, E. M. (1959). Theory of elasticity.
- 1355 Lapusta, N., Rice, J. R., Ben-Zion, Y., & Zheng, G. (2000). Elastodynamic analysis for slow
 1356 tectonic loading with spontaneous rupture episodes on faults with rate-and state-dependent
 1357 friction. *Journal of Geophysical Research: Solid Earth*, *105*(B10), 23765–23789.
- 1358 Le Bouil, A., Amon, A., McNamara, S., & Crassous, J. (2014). Emergence of cooperativity in
 1359 plasticity of soft glassy materials. *Physical review letters*, *112*(24), 246001.
- 1360 Lechenault, F., da Cruz, F., Dauchot, O., & Bertin, E. (2006). Free volume distributions and compactivity
 1361 measurement in a bidimensional granular packing. *Journal of Statistical Mechanics: Theory and Experiment*, *2006*(07), P07009.
- 1362 Lemaître, A. (2002). Rearrangements and dilatancy for sheared dense materials. *Physical Review Letters*, *89*(19), 195503.
- 1363 Li, Q., Tullis, T. E., Goldsby, D., & Carpick, R. W. (2011). Frictional ageing from interfacial
 1364 bonding and the origins of rate and state friction. *Nature*, *480*(7376), 233.
- 1365 Li, T., & Rubin, A. M. (2017). A microscopic model of rate and state friction evolution. *Journal of*
 1366 *Geophysical Research: Solid Earth*, *122*(8), 6431–6453.
- 1367 Lieou, C. K., Daub, E. G., Guyer, R. A., Ecke, R. E., Marone, C., & Johnson, P. A. (2017).
 1368 Simulating stick-slip failure in a sheared granular layer using a physics-based constitutive
 1369 model. *Journal of Geophysical Research: Solid Earth*, *122*(1), 295–307.
- 1370 Ma, X., & Elbanna, A. (2018). Strain localization in dry sheared granular materials: A compactivity-
 1371 based approach. *Physical Review E*, *98*(2), 022906.
- 1372 Mair, K., Frye, K. M., & Marone, C. (2002). Influence of grain characteristics on the friction of
 1373 granular shear zones. *Journal of Geophysical Research: Solid Earth*, *107*(B10), ECV–4.
- 1374 Mair, K., & Marone, C. (1999). Friction of simulated fault gouge for a wide range of velocities and
 1375 normal stresses. *Journal of Geophysical Research: Solid Earth*, *104*(B12), 28899–28914.
- 1376 Makse, H. A., Gland, N., Johnson, D. L., & Schwartz, L. (2004). Granular packings: Nonlinear
 1377 elasticity, sound propagation, and collective relaxation dynamics. *Physical Review E*, *70*(6),
 1378 061302.
- 1379 Makse, H. A., Gland, N., Johnson, D. L., & Schwartz, L. M. (1999). Why effective medium theory
 1380 fails in granular materials. *Physical Review Letters*, *83*(24), 5070.
- 1381 Manning, M. L., Langer, J. S., & Carlson, J. (2007). Strain localization in a shear transformation
 1382 zone model for amorphous solids. *Physical review E*, *76*(5), 056106.
- 1383 Marone, C. (1998a). The effect of loading rate on static friction and the rate of fault healing during
 1384 the earthquake cycle. *Nature*, *391*(6662), 69.
- 1385 Marone, C. (1998b). Laboratory-derived friction laws and their application to seismic faulting.
 1386 *Annual Review of Earth and Planetary Sciences*, *26*(1), 643–696.

- 1389 Marone, C., & Kilgore, B. (1993). Scaling of the critical slip distance for seismic faulting with shear
1390 strain in fault zones. *Nature*, *362*(6421), 618.
- 1391 Marone, C., Raleigh, C. B., & Scholz, C. (1990). Frictional behavior and constitutive modeling of
1392 simulated fault gouge. *Journal of Geophysical Research: Solid Earth*, *95*(B5), 7007–7025.
- 1393 Marone, C., & Saffer, D. (2015). The mechanics of frictional healing and slip instability during the
1394 seismic cycle. In G. Schubert (Ed.), *Treatise on geophysics (second edition)* (Second Edition
1395 ed., p. 111 - 138). Oxford: Elsevier. Retrieved from <http://www.sciencedirect.com/science/article/pii/B9780444538024000920> doi: <https://doi.org/10.1016/B978-0-444-53802-4.00092-0>
1396 .1016/B978-0-444-53802-4.00092-0
1397
- 1398 Marone, C., & Scholz, C. (1989). Particle-size distribution and microstructures within simulated
1399 fault gouge. *Journal of Structural Geology*, *11*(7), 799–814.
- 1400 Masteller, C. C., Finnegan, N. J., Turowski, J. M., Yager, E. M., & Rickenmann, D. (2019). History-
1401 dependent threshold for motion revealed by continuous bedload transport measurements in a
1402 steep mountain stream. *Geophysical Research Letters*, *46*(5), 2583–2591.
- 1403 MiDi, G. (2004). On dense granular flows. *European Physical Journal E–Soft Matter*, *14*(4).
- 1404 Mindlin, R. D. (1949). Compliance of elastic bodies in contact. *J. Appl. Mech., ASME*, *16*, 259–268.
- 1405 Morgan, J. K. (2004). Particle dynamics simulations of rate-and state-dependent frictional sliding of
1406 granular fault gouge. In *Computational earthquake science part i* (pp. 1877–1891). Springer.
- 1407 Morrow, C. A., & Byerlee, J. D. (1989). Experimental studies of compaction and dilatancy during
1408 frictional sliding on faults containing gouge. *Journal of Structural Geology*, *11*(7), 815–825.
- 1409 Murphy, K. A., Dahmen, K. A., & Jaeger, H. M. (2019, Jan). Transforming mesoscale granular
1410 plasticity through particle shape. *Phys. Rev. X*, *9*, 011014. Retrieved from <https://link.aps.org/doi/10.1103/PhysRevX.9.011014> doi: 10.1103/PhysRevX.9.011014
1411 .aps.org/doi/10.1103/PhysRevX.9.011014 doi: 10.1103/PhysRevX.9.011014
- 1412 Murphy, K. A., MacKeith, A. K., Roth, L. K., & Jaeger, H. M. (2019). The intertwined roles of
1413 particle shape and surface roughness in controlling the shear strength of a granular material.
1414 *arXiv preprint arXiv:1902.03280*.
- 1415 Nakatani, M. (2001). Conceptual and physical clarification of rate and state friction: Frictional
1416 sliding as a thermally activated rheology. *Journal of Geophysical Research: Solid Earth*,
1417 *106*(B7), 13347–13380.
- 1418 Ogawa, S. (1978). Multitemperature theory of granular materials. In *Proc. of the us-japan seminar
1419 on continuum mechanical and statistical approaches in the mechanics of granular materials,
1420 1978* (pp. 208–217).
- 1421 Ogawa, S., Umemura, A., & Oshima, N. (1980). On the equations of fully fluidized granular
1422 materials. *Zeitschrift für angewandte Mathematik und Physik ZAMP*, *31*(4), 483–493.
- 1423 Ono, I. K., O’Hern, C. S., Durian, D. J., Langer, S. A., Liu, A. J., & Nagel, S. R. (2002). Effective
1424 temperatures of a driven system near jamming. *Physical review letters*, *89*(9), 095703.
- 1425 Perrin, H., Clavaud, C., Wyart, M., Metzger, B., & Forterre, Y. (2019). Interparticle friction
1426 leads to non-monotonic flow curves and hysteresis in viscous suspensions. *arXiv preprint
1427 arXiv:1904.03918*.
- 1428 Puckett, J. G., & Daniels, K. E. (2013). Equilibrating temperaturelike variables in jammed granular
1429 subsystems. *Physical Review Letters*, *110*(5), 058001.
- 1430 Rathbun, A. P., & Marone, C. (2013). Symmetry and the critical slip distance in rate and state
1431 friction laws. *Journal of Geophysical Research: Solid Earth*, *118*(7), 3728–3741.
- 1432 Rathbun, A. P., Marone, C., Alley, R. B., & Anandakrishnan, S. (2008). Laboratory study of the
1433 frictional rheology of sheared till. *Journal of Geophysical Research: Earth Surface*, *113*(F2).
- 1434 Rice, J. R. (1993). Spatio-temporal complexity of slip on a fault. *Journal of Geophysical Research:
1435 Solid Earth*, *98*(B6), 9885–9907.
- 1436 Rice, J. R. (2006). Heating and weakening of faults during earthquake slip. *Journal of Geophysical
1437 Research: Solid Earth*, *111*(B5).
- 1438 Rice, J. R., Lapusta, N., & Ranjith, K. (2001). Rate and state dependent friction and the stability
1439 of sliding between elastically deformable solids. *Journal of the Mechanics and Physics of
1440 Solids*, *49*(9), 1865–1898.
- 1441 Ruina, A. (1983). Slip instability and state variable friction laws. *Journal of Geophysical Research:
1442 Solid Earth (1978–2012)*, *88*(B12), 10359–10370.

- 1443 Ruina, A. L. (1980). Friction laws and instabilities: a quasi-static analysis of some dry friction
1444 behaviour. *Ph. D. thesis, Division of Engineering, Brown University.*
- 1445 Salerno, K. M., Bolinteanu, D. S., Grest, G. S., Lechman, J. B., Plimpton, S. J., Srivastava, I.,
1446 & Silbert, L. E. (2018). Effect of shape and friction on the packing and flow of granular
1447 materials. *Physical Review E*, 98(5), 050901.
- 1448 Sammis, C. G., & King, G. C. (2007). Mechanical origin of power law scaling in fault zone rock.
1449 *Geophysical Research Letters*, 34(4).
- 1450 Segall, P., & Rice, J. R. (1995). Dilatancy, compaction, and slip instability of a fluid-infiltrated fault.
1451 *Journal of Geophysical Research: Solid Earth*, 100(B11), 22155–22171.
- 1452 Segall, P., Rubin, A. M., Bradley, A. M., & Rice, J. R. (2010). Dilatant strengthening as a mechanism
1453 for slow slip events. *Journal of Geophysical Research: Solid Earth*, 115(B12).
- 1454 Schäfer, J., Dippel, S., & Wolf, D. (1996). Force schemes in simulations of granular materials.
1455 *Journal de physique I*, 6(1), 5–20.
- 1456 Silbert, L. E. (2010). Jamming of frictional spheres and random loose packing. *Soft Matter*, 6(13),
1457 2918–2924.
- 1458 Silbert, L. E., Ertas, D., Grest, G. S., Halsey, T. C., Levine, D., & Plimpton, S. J. (2001). Gran-
1459 ular flow down an inclined plane: Bagnold scaling and rheology. *Physical Review E*, 64(5),
1460 051302.
- 1461 Sleep, N. H. (1997). Application of a unified rate and state friction theory to the mechanics of
1462 fault zones with strain localization. *Journal of Geophysical Research: Solid Earth*, 102(B2),
1463 2875–2895.
- 1464 Sleep, N. H. (2006). Real contacts and evolution laws for rate and state friction. *Geochemistry,*
1465 *Geophysics, Geosystems*, 7(8).
- 1466 Sleep, N. H., Richardson, E., & Marone, C. (2000). Physics of friction and strain rate localization
1467 in synthetic fault gouge. *Journal of Geophysical Research: Solid Earth*, 105(B11), 25875–
1468 25890.
- 1469 Song, C., Wang, P., & Makse, H. A. (2005). Experimental measurement of an effective temperature
1470 for jammed granular materials. *Proceedings of the National Academy of Sciences*, 102(7),
1471 2299–2304.
- 1472 Tsai, J.-C., & Gollub, J. P. (2005). Granular packings sheared in an annular channel: Flow localiza-
1473 tion and grain size dependence. *Physical Review E*, 72(5), 051304.
- 1474 Tullis, T. E., & Weeks, J. D. (1986). Constitutive behavior and stability of frictional sliding of
1475 granite. *Pure and Applied Geophysics*, 124(3), 383–414.
- 1476 van der Elst, N. J., Brodsky, E. E., Le Bas, P.-Y., & Johnson, P. A. (2012). Auto-acoustic compaction
1477 in steady shear flows: Experimental evidence for suppression of shear dilatancy by internal
1478 acoustic vibration. *Journal of Geophysical Research: Solid Earth*, 117(B9).
- 1479 van Hecke, M. (2015). Slow granular flows: The dominant role of tiny fluctuations. *Comptes*
1480 *Rendus Physique*, 16(1), 37–44.
- 1481 Wortel, G., Dauchot, O., & van Hecke, M. (2016). Criticality in vibrated frictional flows at finite
1482 strain rate. *arXiv preprint arXiv:1603.04828*.
- 1483 Wortel, G. H., Dijkstra, J. A., & van Hecke, M. (2014). Rheology of weakly vibrated granular
1484 media. *Physical Review E*, 89(1), 012202.
- 1485 Yin, H. (1993). *Acoustic velocity and attenuation of rocks: Isotropy, intrinsic anisotropy, and*
1486 *stress-induced anisotropy* (Doctoral Dissertation). Stanford University.
- 1487 Zhang, H., & Makse, H. (2005). Jamming transition in emulsions and granular materials. *Physical*
1488 *Review E*, 72(1), 011301.

Supporting Information for “A granular-physics-based view of fault friction experiments”

Behrooz Ferdowsi¹, Allan M. Rubin¹

¹Department of Geosciences, Princeton University, Princeton, NJ 08544, USA

Contents of this file

1. More on the variation of steady-state friction with inertial number
2. The influence of the restitution coefficient
3. The influence of grain size
4. The influence of grain-grain friction coefficient
5. Figure S1
6. Figure S2
7. Figure S3
8. Figure S4
9. Figure S5
10. Figure S6

Corresponding author: B. Ferdowsi, Department of Geosciences, Princeton University, Princeton, NJ 08544, USA (behrooz@princeton.edu)

11. Figure S7

Introduction

This supplementary information file includes extended discussion of the results and supplementary figures for the variation of friction with inertial number, and the influences of restitution coefficient, grain size, and grain-grain friction coefficient, on the transient and steady-state frictional behavior of the sheared granular fault gouge. In this file, we also include a supplementary figure for the behavior of servo-controlled system during a velocity-step (Fig. S2), and another supplementary figure for the behavior of fault gouge with quasi-exponential grain size distribution in velocity-stepping tests (Fig. S7).

More on the variation of steady-state friction with inertial number

We would like to acknowledge that most other numerical studies use a power-law (local granular rheology of the form $\mu_{ss} - \mu_0 = c I_n^\alpha$) to describe the variation of friction with inertial number (or sliding speed) in their studies. However, relative to previous numerical studies, we explore a somewhat lower range of I_n (roughly $10^{-7} - 10^{-2}$, compared to $10^{-5} - 10^0$, which extends to well outside the quasi-static regime). While those previous studies found steady-state friction to have a power-law dependence upon I_n , they are nonetheless consistent with ours in that for the overlapping range of I_n ($\sim 10^{-5} - 10^{-2}$) they can be fit quite well by a logarithmic dependence of friction upon I_n , with a slope not much different than ours [e.g., Hatano, 2007]. It is for values of $I_n \gtrsim 10^{-2}$ in those studies, extending well into the inertial regime of flow, that the steady-state friction curve becomes obviously concave-upward. The steady-state results in Figure 2 of the main paper

differ from previous simulations mostly in extending the range of I_n lower by ~ 2 orders of magnitude. We find the logarithmic dependence to continue to those lower values, while the power-law fits (but not the data, since these don't extent to such low I_n) adopted by previous studies continue to flatten with decreasing I_n .

In Figure S1 below, we show a best fit logarithmic function to our friction data ($\mu_{ss} = c \log I_n + b$, where $c = 0.0055$ and $b = 0.403$) for the range of inertial numbers included for the default model in the paper Fig. 2 ($I_n < 5 \times 10^{-3}$). Although there is indeed some scatter in our data around this line for $I_n < 5 \times 10^{-3}$, it is not obvious that the data are more concave up (indicative of a power law) than concave down. Given this, we believe that an experimentalist would fit such data (for $I_n < 5 \times 10^{-3}$) with a logarithm rather than a power law, which has an additional free parameter. In this figure we also include the friction data of our default model for $I_n \geq 5 \times 10^{-3}$. These data are shown with filled black circles in Figure S1A. It is evident from this figure that at an inertial number $I \sim 10^{-2}$, the friction data start to deviate from the logarithmic fit and develop a concave-up shape. Figure S1B shows the friction data only for $I_n \geq 10^{-4}$. This is the range that is used for fitting a power-law function in the study by Hatano (2007) and Bouzid et al (2013). The black line in Fig. S1B shows a power-law fit ($\mu_{ss} - \mu_0 = c I_n^\alpha$, with $\mu_0 = 0.3538$, $c = 0.3981$ and $\alpha = 0.6562$) to these data. The parameters of this power-law fit fall between the range of parameters obtained by Hatano (2007) [$\mu_0 \approx 0.26$, $c = 0.33$, $\alpha = 0.3$ for his frictional Hertzian model with grain-grain friction coefficient of 0.2] and Bouzid et al. (2013) [$\mu_0 = 0.267$, $c = 1.148$, $\alpha = 1$ for the frictional Hookean model with grain-grain friction coefficient of 0.4]. Our default model is not identical to either of these studies, but the difference between these two published studies suggest

that the power-law fit parameters can be expected to vary somewhat.

The influence of the restitution coefficient

Figs. S3A-B show the evolution of friction coefficient and gouge thickness, respectively, in a systems with the minimum value of restitution coefficient in this study ($e_n = 0.003$), and compare them to the behavior of the default model (with $e_n = 0.98$). The comparison is performed for 1 – 2 orders of magnitude velocity-step increases and 1 order of magnitude velocity-step decrease. The results indicate that velocity-step response of the granular fault gouge is largely independent of the choice of the grain-grain restitution coefficient. A similar observation has been made for other values of the restitution coefficient that are explored here.

For the systems that are generated and confined with different restitution coefficients, we also measured the variations of kinetic energy and the ratio of kinetic energy to the total work done by shearing when shearing phase is initiated. The variations of friction coefficient, gouge thickness, and kinetic energy, as a function of slip distance, are shown in Figure S4A-C, respectively. Figure S4A shows that the choice of the restitution coefficient does not result in any macroscopically significant or any systematically observable change in bulk frictional behavior. The variation of gouge thickness with slip distance shows that in approach to steady-state, there might be subtle differences in gouge thickness in systems at the two ends of the damping regime. The system with minimum restitution coefficient (maximum damping) $e_n = 0.003$ appears to reach steady-state frictional behavior at a slightly more dilated state, compared to the system with maximum restitution coefficient

(minimum damping) $e_n = 0.98$. However, these differences will disappear upon shearing for a longer distance, which is the point at which velocity-steps are performed.

The Kinetic Energy (KE) of the gouge layer is calculated from the sum of the kinetic translational and rotational energies, calculated and summed over all grains in the gouge layer:

$$KE = \sum_{i=1}^{n_p} \frac{1}{2} m_p v_p^2 + \sum_{i=1}^{n_p} \frac{1}{2} I_p \omega_p^2 \quad (1)$$

In Eq. 1, n_p is the total number of grains in the system, and m_p , I_p , v_p , and ω_p are the particle's mass, moment of inertia, translational, and angular velocities, respectively. Following the approach to steady-state friction, the variation of kinetic energy appears to be influenced to some small degree by the choice of the restitution coefficient. The systems with higher restitution coefficient ($e_n = 0.98$) and $e_n = 0.92$) appear to have a larger value of kinetic energy, while the systems with lower restitution coefficient show on average smaller values of kinetic energy.

The influence of grain size

We also ran velocity-step increase and decrease tests with a system with a grain and domain size two orders of magnitude smaller than the default model. The variation of friction and gouge thickness for these simulations are shown and compared to the behavior of the default model in Figure S5 A and B, respectively. The overall frictional and dilatational behaviors of the two systems are similar. The critical slip distance in both cases is $D_c \sim 1.7D_{mean}$. The system with two orders of magnitude smaller grain and domain sizes shows a slightly larger evolution effect compared to the default model in velocity-step increase tests. However, these variations could be potentially due to that

the granular RSF parameters are influenced by the gravity forces that are active in this model. The gravity can change the anisotropic pressure state of the gouge more noticeably (although it is still a small contribution) in this "scaled-down" model compared to the default model.

The response of the gouge thickness in velocity step increase and decrease is shown in Figure S5B. These results also show that except for subtle differences in dilatational response, the behaviors are generally similar to the default model. Furthermore, as for the default model, the magnitude of gouge thickness change following velocity-step increase and decrease appears to be asymmetric, while the frictional response is nearly symmetric for both the default and the scaled-down model.

The influence of grain-grain friction coefficient

To examine the influence of grain-grain friction coefficient on the granular RSF behavior, we further performed velocity-step experiments with systems that are prepared with grain-grain friction coefficients of $\mu_g = 1.0$ and $\mu_g = 5.0$. We remind the reader that the grain-grain friction coefficient in our default model was $\mu_g = 0.5$. Figure S6A and B show the variation of friction coefficient and gouge thickness with slip distance, respectively, following $1 - 2$ and -1 orders of magnitude change in shear velocity in the system with $\mu_g = 1.0$. The results are compared to the behavior of the default model. Figure S6A-B show that frictional and dilatational responses of the system with $\mu_g = 1.0$ follow closely the behaviors of the default model. However, here we observe a larger amount of noise and fluctuations in the variation of friction coefficient with slip distance compared to the default model. The frictional and dilatational behaviors of the system with $\mu_g = 5.0$ are

not shown here, but the behaviors remain similar to the default system, with even higher amounts of noise and larger fluctuations in friction coefficient signal.

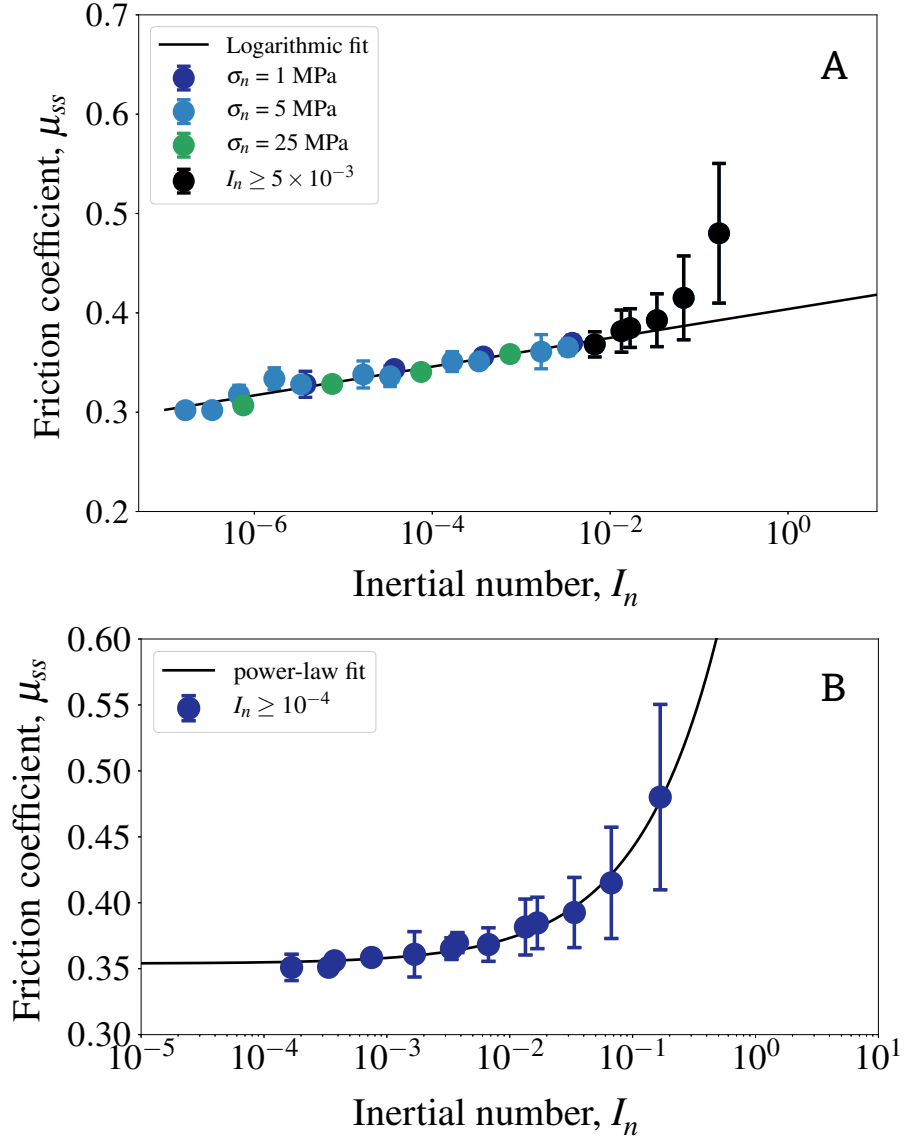


Figure S1. (A) The navy blue, light blue, and green filled circles show the variation of steady-state friction coefficient with inertial number (I_n) for the default system for the range of inertial numbers presented in the manuscript. The black circles show the steady-state friction coefficient with inertial number $I_n \geq 5 \times 10^{-3}$; these are beyond the range of inertial numbers shown in Fig. 2 of the manuscript. The black line shows a logarithmic best fit to the data shown in the paper ($I_n < 5 \times 10^{-3}$). (B) The variation of steady-state friction coefficient with I_n for the default system for $I_n \geq 1 \times 10^{-4}$. This is the range of inertial numbers used in the study by Hatano (2007) and several other granular physics studies for fitting a power-law to the data. The black line shows a power-law best-fit to the data, $\mu_{ss} - \mu_0 = c I_n^\alpha$. The values of the power-law parameters lie between the values found by Hatano (2007) and Bouzid et al. (2013).

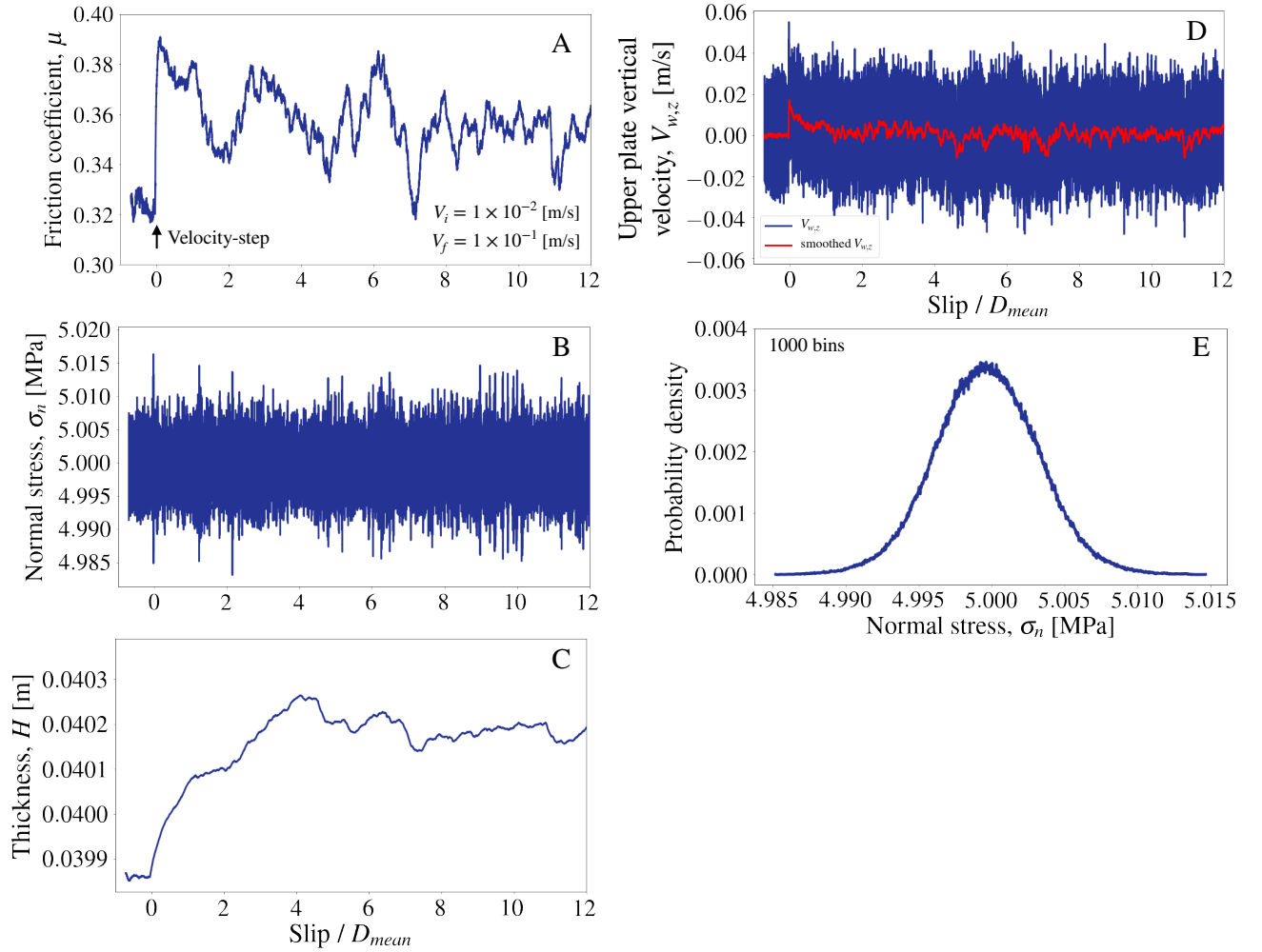


Figure S2. The variation of (A) friction, (B) normal stress, (C) gouge thickness, and (D) upper plate velocity, $V_{w,z}$, with slip distance, in a velocity-stepping test with the initial sliding velocity of $V_i = 10^{-2}$ m/s and the final sliding velocity of $V_f = 10^{-1}$ m/s. Panel (E) shows the probability distribution of normal stress during steady-sliding at $V_f = 10^{-1}$ m/s, for sliding distance $5 \leq \text{Slip}/D_{mean} \leq 12$. All of the signals are sampled every 10 time-steps in the simulation. The smoothed upper plate velocity, $V_{w,z}$ (red line in panel D) is obtained with a moving average with window size $0.01D_{mean}$.

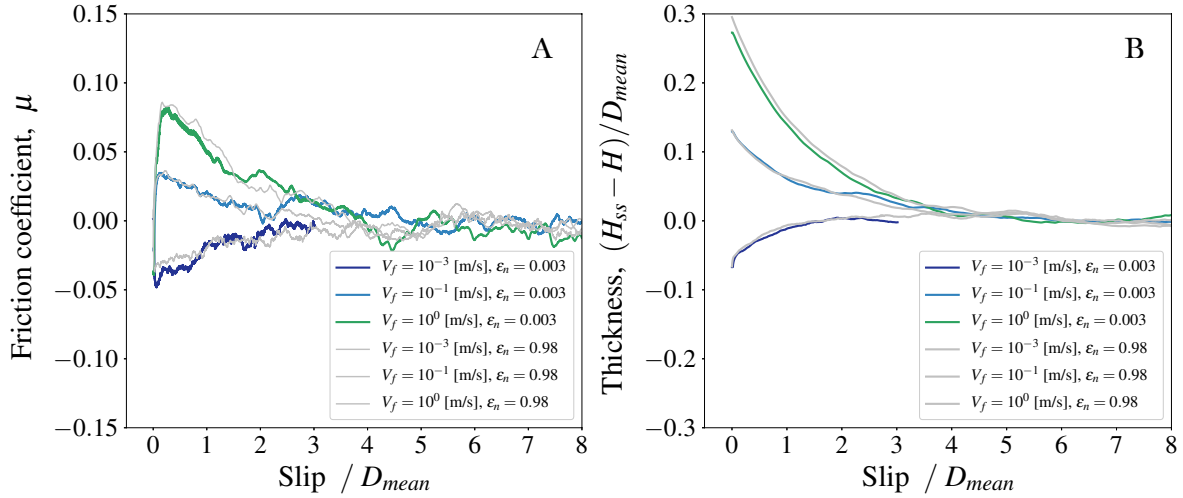


Figure S3. The influence of restitution coefficient on velocity-steps. Panels (A) and (B) show the variation of friction coefficient and gouge thickness with slip distance, respectively, in simulations with 1 – 2 and –1 orders of magnitude change in shear velocity. The initial driving velocity in all tests is $V_i = 10^{-2}$ m/s. The colored lines are simulation results for the system with the restitution coefficient $e_n = 0.003$, whereas the gray lines are the results for the system with $e_n = 0.98$. The results are averaged over seven different realizations. The normal stress is fixed at 5 MPa in all tests.

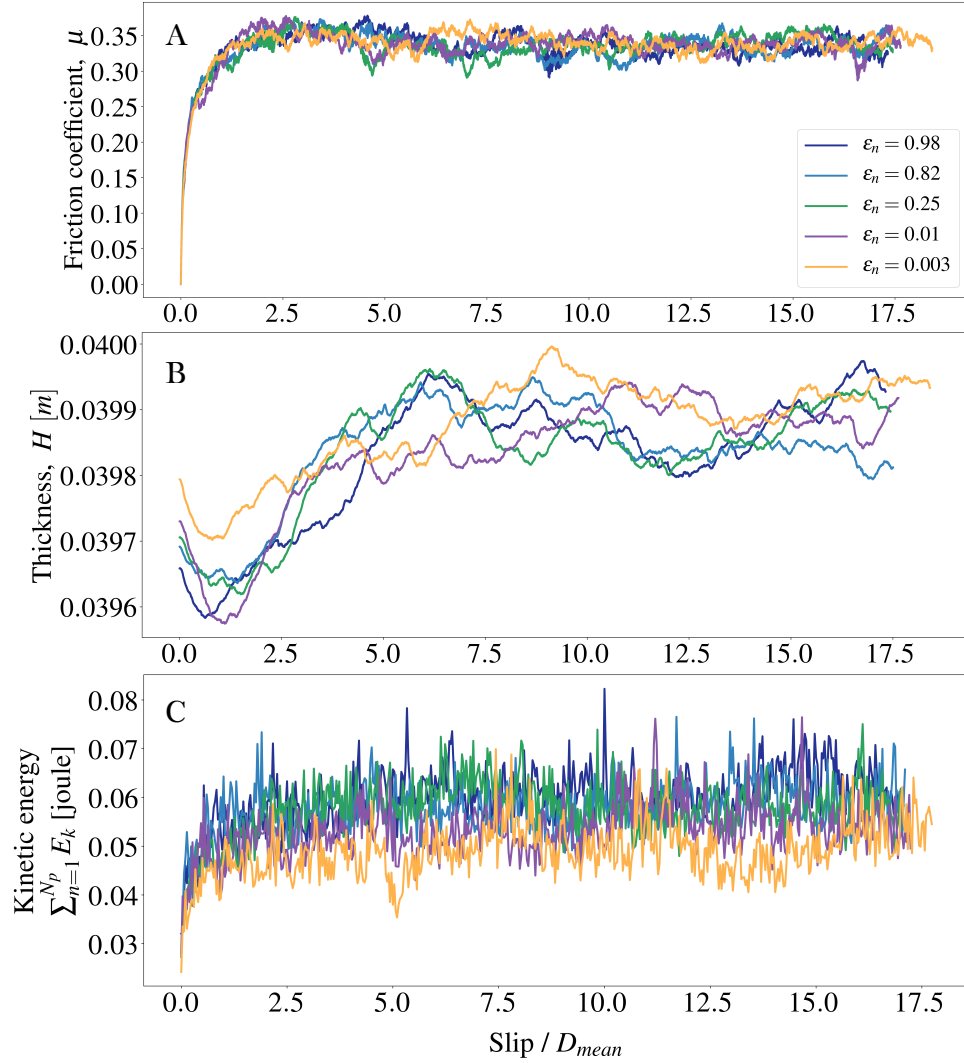


Figure S4. The variation of (A) friction coefficient, (B) gouge thickness, (C) kinetic energy with slip distance for different values of restitution coefficient. The results are only for one realization of the system. The driving velocity is $V_{lp} = 1 \times 10^{-2}$ m/s and the normal stress is fixed at 5 MPa in all simulations.

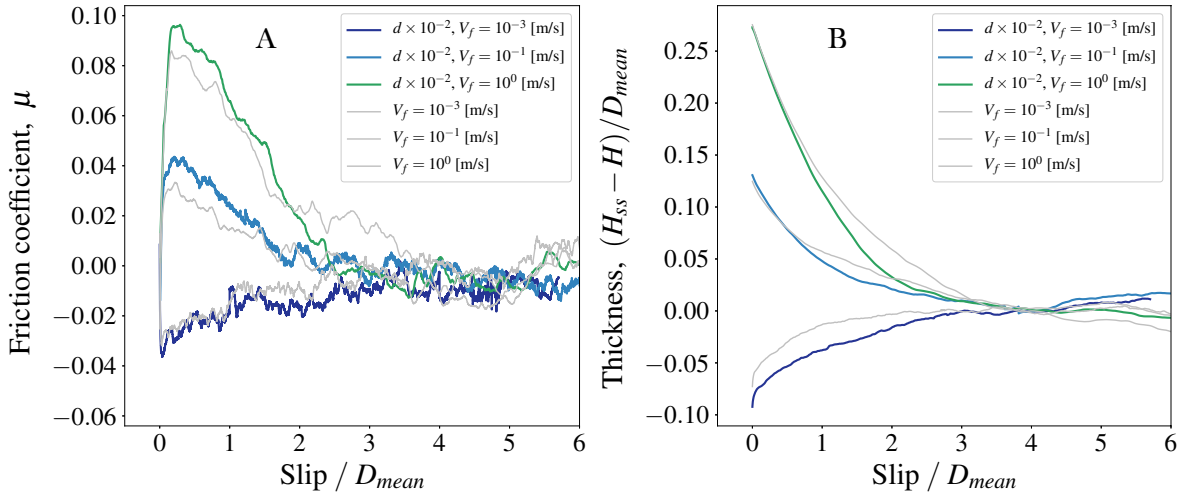


Figure S5. The influence of grain size. Panels (A) and (B) show the variation of friction coefficient and gouge thickness with slip distance, respectively, in simulations with 1 – 2 and –1 orders of magnitude change in shear velocity. The initial driving velocity in all tests is $V_i = 10^{-2}$ m/s. The colored lines are simulation results for the system where grain size is scaled down by two orders of magnitude. The gray lines show the results for the default model. All results are averaged over seven different realizations. The normal stress is fixed at 5 MPa in all tests.

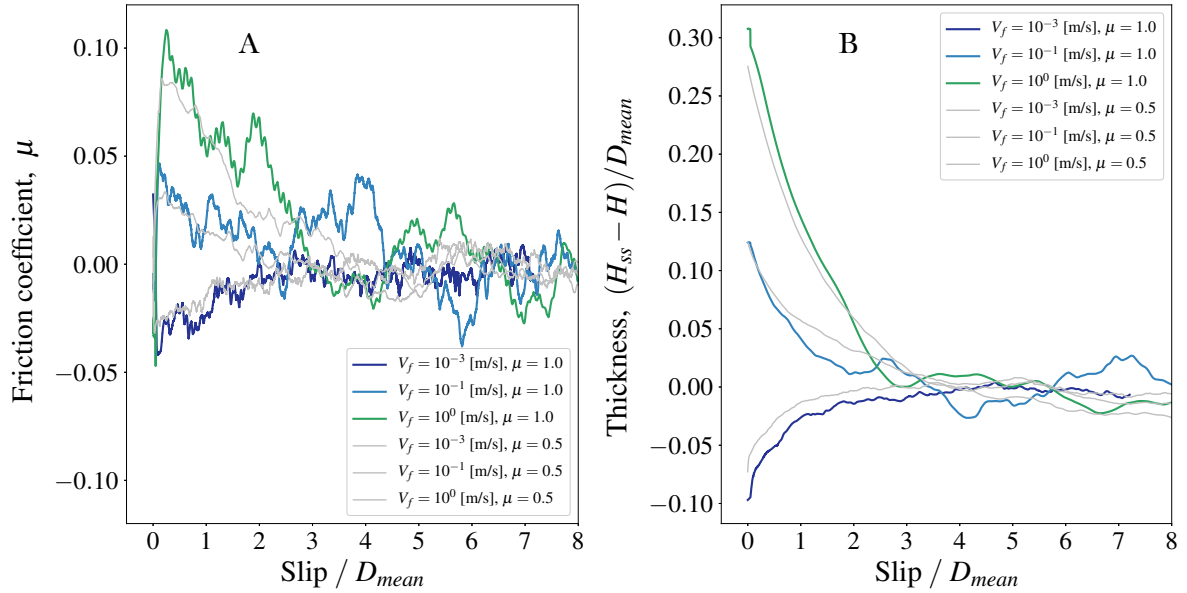


Figure S6. The influence of grain-grain friction coefficient. Panels (A) and (B) show the variation of friction coefficient and gouge thickness with slip distance, respectively, in simulations with 1 – 2 and –1 orders of magnitude change in shear velocity. The initial driving velocity in all tests is $V_i = 10^{-2}$ m/s. The colored lines are simulation results for the system where grain-grain friction coefficient is $\mu_g = 1.0$. The gray lines show the results for the default model. All results are averaged over seven different realizations. The normal stress is fixed at 5 MPa in all tests.

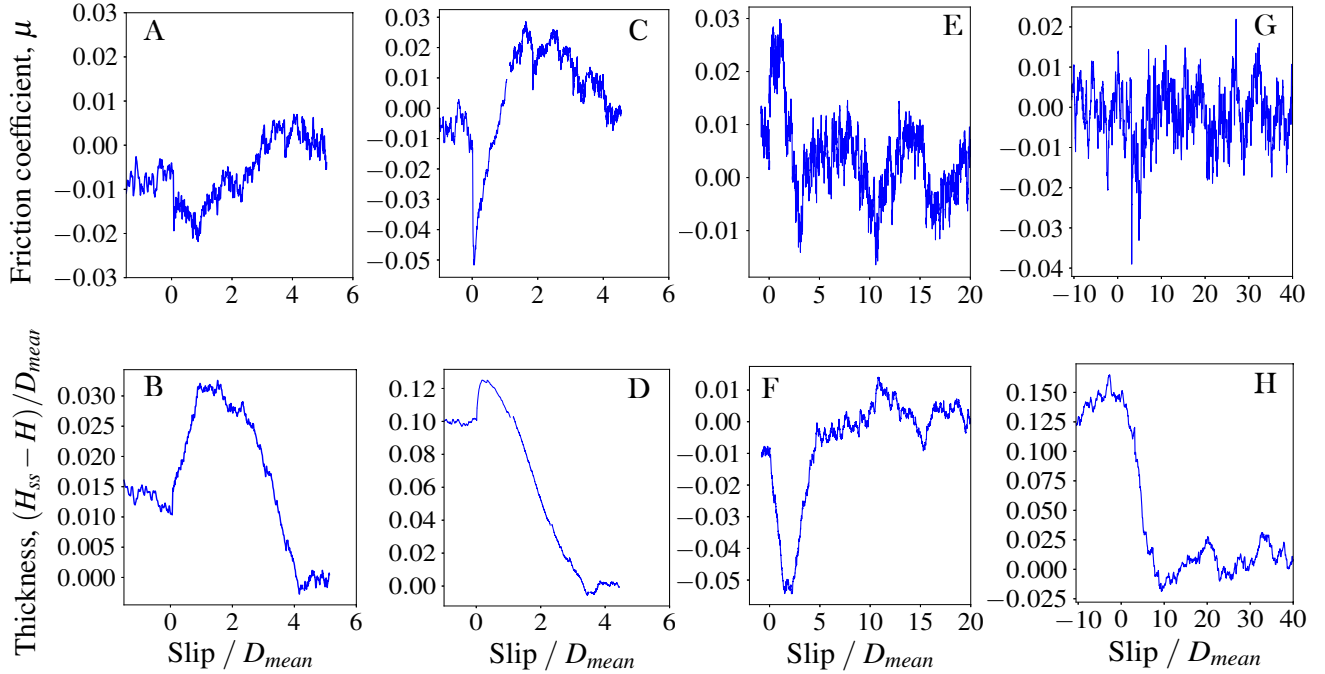


Figure S7. Results of simulations with a quasi-exponential grain size distribution. The top panels (A-C-E-G) show the variation of friction coefficient and the bottom panels (B-D-F-H) show the variation of gouge thickness with slip distance. Panels A-B show results for a 1-order velocity step decrease from $V_i = 10^{-1}$ m/s. Panels C-D show a 2-order step decrease from the same initial velocity. Panels E-F show results for a 1-order velocity step increase from $V_i = 10^{-2}$ m/s. Panels G-H show results for a 1-order step decrease from $V_i = 1$ m/s. $\sigma_n = 5$ MPa. All panels, except G-H, average results from three different realizations; G-H are from a single realization.